Exploring Sequential Reactions and Optical Absorption Processes of Metal Clusters by Employing an Ion Trap

伊藤，智憲

Doctoral Dissertation

Exploring Sequential Reactions and Optical Absorption Processes of Metal Clusters by Employing an Ion Trap

Tomonori Ito

Kyushu University

2015

Acknowledgments

Contents

Chapter 1

General Introduction

1.1 Motivation of metal cluster studies

A metal cluster is a particle which consists of from two to several hundreds of metal atoms. Chemical and physical properties of a cluster, such as reactivity, optical response, magnetism, etc., are different from those of its constituent atom or a corresponding bulk solid of the same element. The characteristic properties originate from its electronic structure, a large surface-to-volume ratio, and confinement of electrons in a nm-scale space. Moreover, a significant feature of the cluster is its size-dependent properties, i.e., properties of the cluster strongly depend on the number of its constituent atoms. These properties have been investigated since 1960s [1], when its unique electronic structure was stated [2].

Nowadays, applications of clusters to materials science are attracting much interest because of their size-dependent properties distinct from each other. For instance, their novel reactivity, which is controllable by size-selection, can be applied to improving catalyst for high efficiency. Although a large amount of data for reactivity of free clusters are available, they may not be applied directly to materials science because there are interaction with, perturbation from, and energy exchange with surroundings in an ambient environment. For example, reactions of transition metal

clusters were investigated as an isolated system under a single-collision condition for elementary-reaction study. A controlled collision energy provides information about thermodynamics of reactions as well [3]. However, sequential reactions, reactivity of hot intermediate in a series of reactions, and termolecular reactions have not been explored intensively, although such reaction processes are often involved in the real world.

1.2 Current status of studies on size-selected free clusters

1.2.1 Reaction experiment

Reactivity and catalytic activity of silver and gold clusters have been investigated by employing an ion trap filled with a buffer He gas [4]. The key advantage of this technique is that a reaction can be observed in the course of energy exchange with the buffer gas. This experimental condition can be regarded as bridging reactions in the gas phase and those in liquid phase. Reactions in liquids or on surfaces represent realistic conditions for investigation of functionality of clusters by *in situ* measurements. However, it is often difficult to elucidate detailed mechanisms without any background knowledge because of the complexity introduced by a large number of atoms involved in the reaction. On the other hand, an ion-trap experiment has an advantage of the gas-phase experiment in that chemical species involved in the reaction can be identified precisely. In addition, environmental effects can be introduced by reactant gases filling the ion trap with controlled partial pressures.

The ion-trap technique has been employed for studies of cluster reactions with a focus on catalytic activities. For example, CO oxidation by free gold, silver, and

binary silver–gold cluster anions [5,6], and methane activation by free Au_2^+ [7,8] are reported. Since these catalytic reactions are dominated by electron transfer from the clusters to the molecules, their reactivity would be changed once the cluster is supported on a substrate or embedded in a liquid or a matrix, i.e., in the presence of surroundings. Therefore, a systematic study of effects of surroundings is essentially important for practical use of clusters in the new stage of cluster-catalyst development in future. In addition, geometrical structures of reactant clusters play an important role in catalytic reactions because these processes are induced by particular reaction sites of catalysts. In this regard, investigations of reactive sites and perturbation effects by employing the ion-trap technique would be fascinating subjects in cluster science.

1.2.2 Spectroscopic measurement

Experiment in the presence of a buffer He gas brings benefits not only to the reaction measurements but also to spectroscopic measurements of size-selected free clusters. Conventionally optical absorption was measured in rare-gas matrices [9, 10] or in ion beams [11–17]. The former method has an advantage in that a number density of the cluster can be increased by extending the deposit duration, although the clusters are strongly perturbed by the matrix. The latter method, on the other hand, provides clusters free from any perturbation of surroundings. However, it is difficult to calculate the number density because of uncertainty in spacial extent of the ions. Therefore, absorption cross sections were reported not as absolute values but as relative ones. By applying an experimental technique employing an ion trap as described in Subsection 1.2.1, photoabsorption can be measured with an accurate number density of cluster ions. Furthermore, temperature of the cluster can be controlled through equilibrium with a buffer gas. The density measurement and

the temperature control, which were not accessible in the previous studies, are now achievable by employing an ion trap.

1.3   Present study

The present study has been conducted to investigate reactions and optical properties of metal clusters by taking the advantage of an ion trap. The author demonstrates the advantages of the methodology by several experiments. First, oxidation processes of transition metal clusters are examined for chromium cluster cations, as described in Chapter 3. Reaction kinetics and sequential reaction pathways are identified by reaction-rate measurement based on variable storage time of ions in the trap. Second, in Chapter 4, adsorption kinetics of inert molecules is investigated to elucidate reaction sites on clusters, which represents a primary step of chemical reactions reflecting a charge distribution in the cluster and accessibility of molecules on the cluster. Adsorption of nitrogen molecules on silver cluster cations is examined for basic example. Third, in Chapter 5, a coadsorption effect of foreign molecules on adsorption kinetics is presented for the gold dimer cation, which is inert otherwise. This experiment demonstrates a systematic study of influence of surrounding molecules, e.g., charge transfer, on chemical properties of clusters. Finally, in Chapter 6, optical excitation processes of silver clusters are investigated with a focus on size dependence. The major interest is to observe a change in optical processes by size: from single-electron excitation in small sizes to collective excitation of electrons, so-called a plasmon resonance, in large sizes. The two processes are distinguished by evaluating photoabsorption cross sections, and thus oscillator strengths, quantitatively. All these experiments were materialized by author's unique experimental technique employing an ion trap.

Chapter 2

Experimental and Computational Methods

Experimental apparatus

Overview

A schematic view of experimental the apparatus is shown in Figure 2.1. It is composed of a series of vacuum chambers including a magnetron-sputtering ion source, two quadrupole mass spectrometers, and a UV-Vis laser system. The chambers are differentially evacuated by turbo-molecular pumps supported by rotary pumps, and the pressure typically reaches to the order of 10^{-5} Pa. The chambers contain octopole ion guides, quadrupole deflectors, and ion lenses for the transportation of cluster ions. Cluster ions produced from the ion source were guided by the ion optics and mass-selected by the quadrupole mass filter (MAX-16000, Extrel CMS), and were introduced into a 40-cm long linear ion trap, which is composed of eight rods as well as the ion guides. In order to shorten ion-loading time and let the ions be localized near the center of the electrode [18], the ion trap was used as a quadrupole type by wiring adjacent electrodes. The cluster ions interacted with reactant molecules or the laser pulses during beingtrapped. The extracted ions from

the trap were mass-analyzed by the second quadrupole mass spectrometer (MAX-4000, Extrel CMS), and were detected as ion current by a high sensitivity ammeter (Picoammeter 6485, Keithley).
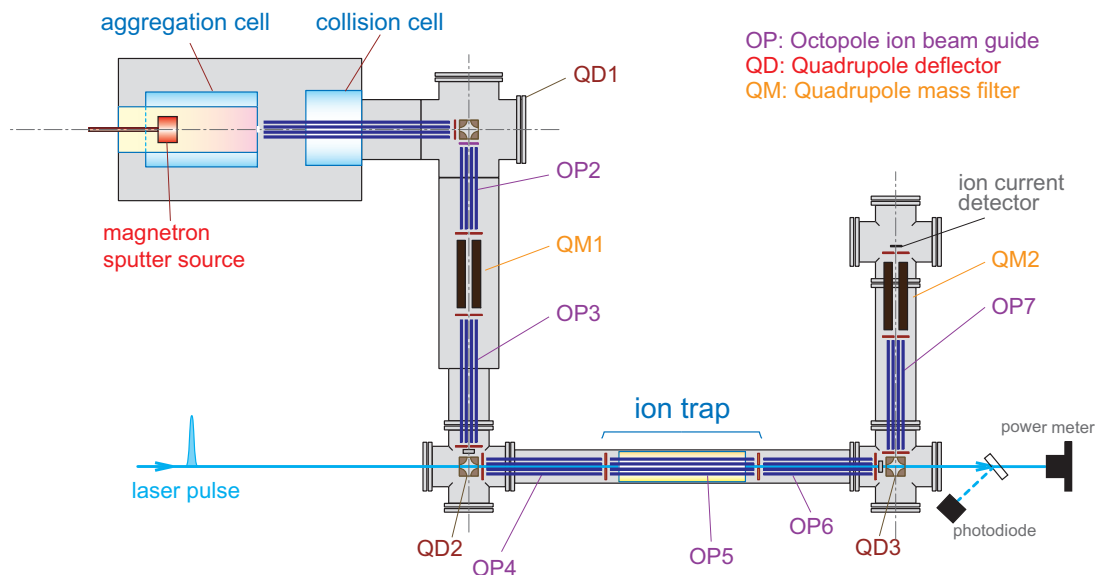
Figure 2.1: Schematic diagram of the experimental setup.

Cluster ion source

Metal cluster cations, M_n^+, were produced by the magnetron-sputtering ion source, which is enclosed within an aggregation cell filled with a buffer He gas. Metal targets were sputtered by Ar cations, which were obtained by electric discharge using a DC power supply (MDX, Advanced energy). Flow rates of the He gas and the Ar gas were controlled by mass flow controllers (MODEL 3650 Series, KOFLOC), set typically to be 300 and 100 SCCM, respectively. Sputtered metal atoms were extracted in the aggregation cell and collide with the buffer He, which was cooled with liquid nitrogen. As a result of collisions with the buffer He, metal atoms and ions lost their energies to form clusters because the kinetic energy of constituent atoms must

6

be smaller than binding energy of the cluster. The produced clusters pass through a collision cell, which is located immediately downstream of the aggregation cell. The collision cell was used to stabilize the clusters in the ground state and attach preadsorption molecules on the clusters.

Ion guide

All the ion species were guided by radio-frequency (rf) octopole ion guides (denoted by OP in Figure 2.1), which consist of eight electrode rods. Sources of rf voltage are LC-resonant type circuits [19]. Inductance of homemade coils and capacitance of the ion guides correspond to L and C of the LC-resonant circuit, respectively. Frequencies of the ion guides are tuned by changing numbers of turns in the coils.

Laser system

A UV laser was applied for the optical absorption spectroscopic measurement. The UV laser was generated by frequency doubling of a tunable dye radiation (Scanmate 2E, Lambda Physik) pumped by a XeCl excimer laser (COMPex, Lambda Physik). The output of the XeCl laser was typically 150 mJ per pulse at a 10-Hz repetition. The output of the dye laser was frequency-doubled in a BBO crystal for the tunable UV laser source. Intensity of the laser was monitored at the most downstream by a power meter (Thermal Sensor 3A-P, Ophir) in order to calculate the number of incident photons, n_{photon}. Below the detection limit of the power meter (60 μW), the incident-light power was calculated from the intensity of a portion of the laser, which was measured by a photodiode with a calibration relation between the power meter and the photodiode reading.

Computation

In order to supplement experimental results, quantum chemical calculations were performed using density functional theory (DFT). Geometrical structures and relative energies of clusters and their adducts were obtained in the calculations. In addition, a vibration analysis was performed for all of the obtained structures in order to confirm that the structures are minima on the potential energy surfaces. For assignments of optical spectra, electronic transitions were calculated using spin unrestricted time-dependent DFT (TD-DFT) considering 500 excited states. All calculations were performed using the Gaussian09 program [20].

Chapter 3

Multistep Reaction Kinetics Measurements in Oxidation of Chromium Cluster Cations

3.1 Introduction

Chromium shows various properties when it is bound to oxygen. For instance, chromium in stainless steel forms passive films with oxygen in air, which show corrosion resistance. Alteration in magnetic properties by oxygen is also characteristic of chromium, which by itself exhibits antiferromagnetism in bulk. One form of oxide compounds, Cr_2O_3, is an antiferromagnetic insulator, whereas another form, CrO_2, is ferromagnetic and metallic [21]. In the gas-phase isolated clusters, it has been shown that the chromium dimer anion $Cr_2{}^-$, which is in the low-spin doublet ground state, $^2\Sigma_u^+$ [22], turns to a high-spin state when it is oxidized to form $Cr_2O_n{}^+$ (n = 1–3) [23, 24]. Furthermore, theoretical calculations report that successive addition of oxygen atoms to Cr_2 leads to oscillatory change in the magnetic moments of Cr_2O_n (n = 0–6) [25, 26]. It should be noted that chromium shows various oxidation numbers. Compounds of element chromium show a variety of colors depending on their oxidation numbers, as rightly named after "color" in Greek. Number +3 is

the most stable among them, which causes the dichromic acid ion, $Cr_2O_7^{2-}$, and the chromic acid ion, CrO_4^{2-}, both being effective oxidizing agents. Gas-phase chromium oxide clusters are formed as well with a wide range of compositions; see Refs. [27] and [28] for neutral and cationic clusters, respectively. Substoichiometric (oxygen-deficient) oxide clusters are produced in reactions under low partial pressure of oxygen, while fully-oxidized ones are generated under oxygen-rich conditions. This chapter presents oxidation reactions of chromium cluster cations, Cr_2^+ and Cr_3^+, with O_2 molecules. The production mechanisms and stabilities of chromium oxide clusters are investigated by experiments employing the ion trap. Chromium cluster ions are confined in the ion trap with O_2 gas in the measurement for a variable time to analyze the reaction products as a function of the storage time. This enables me to study the kinetics of multistep reactions in multiple-collision conditions [29]. The kinetics measurement has also been performed for an oxidized cluster, Cr_2O^+, which appears as a reaction intermediate in the oxidation process. The kinetics of the intermediate Cr_2O^+ is compared with that of cold Cr_2O^+ generated in the cluster source to discuss the thermalization process of the product ions in collision with the buffer gas in the trap. The ion trap has provided studies of temperature dependence as well.

3.2   Experimental procedure

The experimental setup has been described in detail in Chapter 2 or elsewhere [30]. Briefly, chromium cluster cations, $Cr_n{}^+$, were generated by the magnetron-sputtering ion source, followed by aggregation through collisions with a He gas cooled by liquid nitrogen. For production of oxide cluster ions, $Cr_nO_m^+$, O_2 gas was introduced along with N_2 gas to the liquid-nitrogen-cooled collision cell located

immediately downstream of the cluster source. The ions were mass-selected by a quadrupole mass filter and guided to a 40-cm linear radio frequency (rf) ion trap. The ion current of the mass-selected clusters depended on the size and composition, and ranged between 100 and 600 pA as measured by a current meter for the target ions. Buffer He gas was introduced continuously into the ion trap for deceleration and thermalization of the ions. Reactant O_2 gas was mixed with the buffer He gas for reaction experiments. The mass-selected ions were introduced into the ion trap for 100-ms loading time, and eventually $\sim 5 \times 10^7$ ions were stored. The end of the loading was defined as the origin of the storage time ($t = 0$). The ions were extracted after a given storage time and analyzed by a second quadrupole mass filter. The amounts of product and reactant ions were measured as a function of the storage time t. Note that a small amount of reaction products, which was produced during ion loading, was present already at $t = 0$. The total amounts of the stored ions decreased with the storage time, because Coulomb repulsion between the ions forced them to escape the trap; it decreased by $\sim 10\%$ after 600 ms. Therefore, the data were calibrated for this systematic ion loss by normalizing the total amount of ions to the value measured at $t = 0$ ms. The temperature of the ion trap, monitored by a carbon resistance thermometer for temperature-dependence studies, was cooled down to 100 K by liquid nitrogen. At the ion current of 600 pA, $\sim 4 \times 10^8$ ions should be introduced within the 100-ms ion loading time. However, the measured current of the ions extracted from the trap indicated that the actual numbers of the stored ions, $\sim 5 \times 10^7$, was less than the injected ions. This implied that the ion trap is fully filled after reaching the space-charge limit and thus provided a constant load of ions. To reach this saturation condition relatively fast, the present linear ion trap, consisting of eight electrode poles, was modified to form a quadrupole configuration by wiring two adjacent poles connected. In this way, the trap volume was reduced

11

in comparison with an octopole configuration [18] so as to shorten the loading time for saturation. In the reaction experiment, the partial pressures of He and O_2 in the ion trap were adjusted to be in the orders of 10^{-1} and 10^{-5} Pa, respectively; these pressures correspond to the collision rates of 1×10^4 and 2 s^{-1}, respectively, where the collisional cross sections are estimated by the Langevin-Gioumousis-Stevenson model, $\sigma_{\mathrm{LGS}} = \pi e \left(2\alpha/E\right)^{1/2}$ [31]. Here, a stands for polarizability of the target gases (0.205 and 1.58 Å^3 for He and O_2, respectively), e is the charge on the ion, and E is the collision energy in the center-of-mass frame. In this partial pressure condition, where the collisional rate with He is much higher than that with O_2, it was presumed that the reaction products are thermalized before subsequent reaction with the second O_2 molecule.

3.3   Results

3.3.1   Reaction of Cr$^+$ with O$_2$

The atomic ion, Cr$^+$, did not produce any product ions with oxygen molecules during trapping. This is consistent with the fact that the reaction of Cr$^+$ with the triplet oxygen $\left(^3\Sigma_g^-\right)$ in the ground electronic state is endothermic [32] with a reaction threshold of 1.40 $\pm$ 0.12 eV [33]; it is reported that Cr$^+$ reacts only with the singlet oxygen $\left(^1\Delta_g\right)$ at room temperature [34]. Under the present experimental condition, the initial collision energy with O_2 of the chromium cation was 2.6 eV in the center-of-mass frame, but they were decelerated by collision with a buffer He gas after injection into the ion trap. This is probably the reason for that Cr$^+$ does not react with O_2 under the present condition. With reference to molecular dynamics simulations [35], 40 collisions with He atoms (3-ms trapping) are sufficient

12

for reduction of the translational energy of Cr^+ below the reaction threshold (detail calculation is discussed in Subsection 6.4.1).

3.3.2 Reaction of Cr_2^+ with O_2

The temporal evolution of the reaction of Cr_2^+ with O_2 is shown in Figure 3.1. Figure 3.1b shows the same plots magnified by a factor of 100 in the ion intensity. Each data point is an average over ten repeated measurements. The error bars represent estimated statistical uncertainties of the measurements in one standard deviation, whereas systematic uncertainties are larger ($\sim$ 20%); see 3.4.1. In the reaction of $Cr_2^+ + O_2$, four reaction products, i.e., Cr_2O^+, CrO_2^+, CrO^+, and Cr^+, are reported to be produced by a single collision [28]. The present multiple-collision experiment also produced these ions, while oxygen-rich ions such as $Cr_2O_6^+$ and $Cr_2O_7^+$ were not observed, although such ions are reported to be produced under oxygen-rich conditions in the ion source [36]. The time evolution of the reactant intensity showed a single-exponential decay. The main products, Cr^+ and CrO^+, increased monotonically. Their production ratio, $[Cr^+]/[CrO^+]$, was 3.42 $\pm$ 0.04 throughout the storage time. It should be noted that the formation of Cr^+ from Cr_2^+ is ascribed solely to the reaction with an oxygen molecule excluding collision-induced dissociation. As estimated for the present Cr_2^+, which was injected into the ion trap at a center-of-mass collision energy of 1.5 eV against O_2, 10 collisions with buffer He gas (corresponding to 0.7-ms residence time in the ion trap) are sufficient to reduce the energy below the bond energy (1.30 $\pm$ 0.06 eV) of Cr_2^+ [37]. Cr_2O^+ is assigned in Figure 3.1b to an intermediate product, because it shows the maximum intensity at t = 400 ms and disappears as the time elapses, whereas the amount of CrO_2^+ increases continuously. Similar measurements at an ion-trap temperature of 120 K resulted in nearly equal rate constants of kinetics. This implies that these

13

reactions have very low reaction barriers, as is general for ion–molecule reactions.

3.3.3 Reaction of Cr_3^+ with O_2

The kinetics of Cr_3^+ in the reaction with O_2 is shown in Figure 3.2 a, along with Figure 3.2 b in a magnified scale. Among the seven products reported for single-collision reactions, Cr_3O^+, $Cr_2O_2^+$, Cr_2O^+, Cr_2^+, CrO_2^+, CrO^+, and Cr^+ [28], five of them were observed in the present measurement; the formation cross sections for Cr_3O^+ and CrO_2^+ are too small to be detectable. Oxygen-rich products such as $Cr_3O_8^+$ were not observed, as in the Cr_2^+ case. The number of Cr_3^+ decreased exponentially with the storage time. The final products were Cr^+ and CrO^+. The formation rate of the latter was lower than that of the former. The production ratio of $[Cr^+]/[CrO^+]$ decreased from 6.2 at t = 0 ms to 2.9 at t = 800 ms; the latter was similar to that obtained for the Cr_2^+ + O_2 reaction. Other products, Cr_2O^+, Cr_2^+, and Cr_2O^+, which are reaction intermediates, reached the maximum intensities at $t = 100$ ms. The data at t = 0 ms show that 40% of the reactant ion, Cr_3^+, had already undergone reaction within the loading time similar to the Cr_2^+ experiment. This suggests that the reaction cross section of Cr_3^+ is larger than that of Cr_2^+. The kinetics was independent of the temperatures down to 120 K.

3.3.4 Reactions of chromium oxide cations, CrO^+ and Cr_2O^+

It was confirmed that CrO^+ did not generate any products with O_2 in the trap. This is expected because CrO^+ is the most stable among the chromium oxide cluster cations [38]. On the other hand, Cr_2O^+ produced Cr^+ and CrO^+ as shown in Figure 3.3. The reactant decreased exponentially with the storage time, while the products increased monotonically. The ratio of Cr^+ to CrO^+ had a constant value of 2.36 ±

14

0.02 over the present storage time.

3.4 Discussion

3.4.1 Reaction mechanism of Cr_2^+ with O_2

The following four exothermic reaction paths have been reported for the reaction of Cr_2^+ with O_2 [28], where the heat of reaction is listed in eV:

$$Cr_2^+ + O_2 \quad \rightarrow \quad Cr^+ + CrO_2 \quad -3.36 \pm 0.63 \qquad (3.1)$$

$$CrO^+ + CrO \quad -1.81 \pm 0.22 \qquad (3.2)$$

$$Cr_2O^+ + O \quad -0.16 \pm 0.17 \qquad (3.3)$$

$$CrO_2^+ + Cr \quad -0.17 \pm 0.82 \qquad (3.4)$$
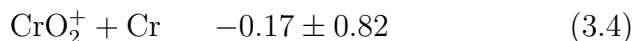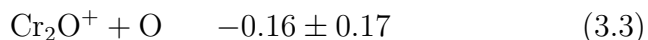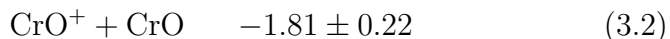
As shown in Figure 3.1, Cr^+ and CrO^+ in Eqs. (3.1) and (3.2) were the major final products observed in the experiment. In contrast, Cr_2O^+ in Eq. (3.3) was identified as an intermediate, which reacted further with O_2 to the final product ions. The branching fraction to CrO_2^+ in Eq. (3.4) was less than 1% of the total reaction paths. Based on the above elementary reactions, the reaction pathways illustrated in Figure 3.4 a were derived. The analysis was carried out by fitting the data to integrated rate equations. The number density of continuously flowing O_2 ($\sim 5 \times 10^{15}$ m^{-3}) was much higher than that of the ions ($< \sim 1.2 \times 10^{12}$ m^{-3}). Therefore, the concentration of O_2 is assumed to be constant in the analysis; i.e., each reaction is treated as a pseudo-first-order process. In Figure 3.4, $k_{(n,m \rightarrow n',m')}$ represents the rate constant of $Cr_nO_m^+$ to produce $Cr_{n'}O_{m'}^+$. A prime on the k represents the reaction rate of an intermediate product. A double prime stands for that of a secondary intermediate.

On the basis of pseudo-first-order rate equations, the temporal evolution of the amount of the reactant ion is expressed as

$$\left[\mathrm{Cr_2}^+\right] = \left[\mathrm{Cr_2}^+\right]_0 \exp\left\{-k_{(2,0)}\left(t+t_0\right)\right\}, \tag{3.5}$$

where $[\mathrm{Cr_2^+}]_0$ is the initial amount at $t = -t_0$, and $k_{(2,0)}$ stands for the summation of the rate constants of all the reactions from $\mathrm{Cr_2^+}$. The parameter t_0 takes into account the fact that the reactions partially start before $t = 0$ during the ion loading. For the intermediate product $\mathrm{Cr_2O^+}$, its integrated rate equation is given by

$$\left[\mathrm{Cr_2O^+}\right] = \left[\mathrm{Cr_2}^+\right]_0 \frac{k_{(2,0\to2,1)}}{k'_{(2,1)} - k_{(2,0)}}\left[\exp\left\{-k_{(2,0)}\left(t+t_0\right)\right\} - \exp\left\{-k'_{(2,1)}\left(t+t_0\right)\right\}\right], \tag{3.6}$$

where $k'_{(2,1)}$ stands for the total rate constant of the intermediate $\mathrm{Cr_2O^+}$, i.e.,

$$k'_{(2,1)} \equiv k'_{(2,1\to1,0)} + k'_{(2,1\to1,1)} \tag{3.7}$$

There are two paths leading to the final product $\mathrm{Cr^+}$; one is the route directly from $\mathrm{Cr_2^+}$ and the other is via the intermediate $\mathrm{Cr_2O^+}$. Consequently, the time dependence of the amount of the final product $\mathrm{Cr^+}$ is written by

$$
\begin{aligned}
\left[\mathrm{Cr^+}\right] =\ & \left[\mathrm{Cr_2}^+\right]_0 \left[-\frac{k_{(2,0\to2,1)}\left(k'_{(2,1)} - k_{(2,0)}\right) + k_{(2,0\to2,1)}k'_{(2,1\to1,0)}}{k_{(2,0)}\left(k'_{(2,1)} - k_{(2,0)}\right)} \exp\left\{-k_{(2,0)}\left(t+t_0\right)\right\} \right.\\
& + \frac{k_{(2,0\to2,1)}k'_{(2,1\to1,0)}}{k'_{(2,1)}\left(k'_{(2,1)} - k_{(2,0)}\right)} \exp\left\{-k'_{(2,1)}\left(t+t_0\right)\right\}\\
& \left. + \frac{k_{(2,0\to2,1)}k'_{(2,1\to1,0)} + k_{(2,0\to1,0)}k'_{(2,1)}}{k_{(2,0)}k'_{(2,1)}} \right]
\end{aligned}
\tag{3.8}
$$

16

The amount of the other final product, CrO^+, can be expressed by replacing $k_{(2,0\to1,0)}$ and $k'_{(2,1\to1,0)}$ in Eq. (3.8) with $k_{(2,0\to1,1)}$ and $k'_{(2,1\to1,1)}$, respectively. The experimental data in Figure 3.1 were reproduced by the fitting curves superimposed by solid lines. The rate constants thus obtained by the fitting procedure are listed in Table 3.1. The rate constants indicate that most of the final products were directly gen-

Table 3.1: Pseudo-first-order rate constants, k, and the reaction cross sections, σ, of each step of elementary reactions.
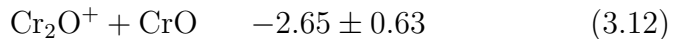
Reactant and product ion	k_{p} / s^{-1}	$\sigma(300\ \mathrm{K})$ / Å^2
(3.1) $Cr_2^+ \to Cr^+$	1.62 (1)	44.4 (4)
(3.2) $Cr_2^+ \to CrO^+$	0.480 (4)	13.1 (1)
(3.3) $Cr_2^+ \to CrO_2^+$	0.0066 (2)	0.18 (1)
(3.4) $Cr_2^+ \to Cr_2O^+$	0.071 (3)	1.95 (9)
(Product in 3.4) $Cr_2O^+ \to Cr^+$, CrO^+	3.1 (8)	86 (21)

erated from Cr_2^+; those produced via an intermediate Cr_2O^+ were 3%. The total reaction rate constant, $k'_{(2,1)}$, of Cr_2O^+ was determined to be 3.1 ± 0.8 s^{-1}, which is comparable to that of Cr_2^+, $k_{(2,0)}$ (= 2.18 ± 0.01 s^{-1}). The amount of Cr_2O^+ was so small that the branching ratio of $k'_{(2,1\to1,0)}$ to $k'_{(2,1\to1,1)}$ could not be determined. This issue will be discussed in 3.4.2. The thermal rate constant, γ, of gas-phase reactions is generally expressed as, where v is the relative velocity between the reactant molecules and the brackets represent an average over the thermal velocity, since the reaction cross section, σ, depends on the translational energy of the reactants. In ion–molecule reactions, however, the rate constant is independent of the velocity because of the general $1/v$-dependence of $\sigma(v)$, and therefore no longer depends on the temperature. Hence, the reaction cross section $\sigma_{(n,m\to n',m')}$ is related to the pseudo-first-order rate constant as $k_{(n,m\to n',m')} = [O_2]\,v\sigma_{(n,m\to n',m')}$ without averaging over the velocity distribution [39], where $[O_2]$ is the number density of O_2.

The cross sections evaluated from this relation are listed in Table 3.1 along with the pseudo-first-order rate constants. Here, the density $[O_2]$ was calibrated by referring to the total reaction cross section of Cr_2^+ with O_2 reported by single-collision experiment [28]; the other cross sections were determined by using the O_2 concentration thus evaluated. Therefore, the cross sections are associated with systematic uncertainties of $\sim 20\%$ as reported [28], although the statistical errors in the present measurement are much smaller. The cross sections in Table 3.1 are similar to those reported in Ref. [28] except that of Cr_2O^+ formation. The formation cross section of Cr_2O^+, which was a reaction intermediate in the present multiple-collision condition, may be underestimated because the successive secondary reaction was found to be much faster than its formation.

3.4.2 Reaction mechanism of Cr_3^+ with O_2

As for the reaction of $Cr_3^+ + O_2$, 23 reaction paths and their heats of reaction have been reported [28]. Among them, the products observed in the present measurement are generated as follows, where the heats of reaction are listed in eV:

$$
\begin{aligned}
Cr_3^+ + O_2 \quad \rightarrow \quad & Cr^+ + Cr_2O_2 & < -1.56 & \qquad (3.9) \\
& CrO^+ + Cr_2O & < -2.35 & \qquad (3.10) \\
& Cr_2^+ + CrO_2 & -1.87 \pm 0.22 & \qquad (3.11) \\
& Cr_2O^+ + CrO & -2.65 \pm 0.63 & \qquad (3.12) \\
& Cr_2O_2^+ + Cr & < 0 & \qquad (3.13)
\end{aligned}
$$
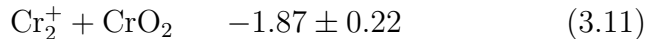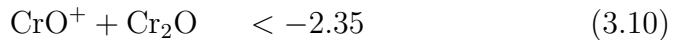
As shown in Figure 3.2, Cr^+ and CrO^+ were the final products as in the case of the $Cr_2^+ + O_2$ reaction. Products in Eqs. (3.11)–(3.13) are intermediates, which

undergo further reactions. Among these intermediates, $Cr_2{}^+$ and Cr_2O^+ follow the same reaction paths as those described in 3.4.1. The amount of CrO_2^+ (see Eq. (3.4)), which should be produced from $Cr_2{}^+$ as a final product, was too small to be detectable; it was thus ignored in the analysis of reaction kinetics. The reaction pathways found in the present experiment are illustrated in Figure 3.4b. The experimental data in Figure 3.2 were reproduced by the fitting curves superimposed by the solid lines, which were obtained by the procedure similar to that of $Cr_2{}^+$. The rate constants and the reaction cross sections corresponding to each reaction step are summarized in Table 3.2. The total reaction cross section of $Cr_3{}^+$, found to be

Table 3.2: Pseudo-first-order rate constants, k, and the reaction cross sections, σ, of each step of elementary reactions.

Reactant and product ion	k_{p} / s^{-1}	$\sigma(300 \text{ K})$ / Å^2
(3.9) $Cr_3^+ \rightarrow Cr^+$	4.3 (3)	61 (5)
(3.10) $Cr_3^+ \rightarrow CrO^+$	0.26 (6)	3.7 (8)
(3.11) $Cr_3^+ \rightarrow Cr_2^+$	0.312 (8)	4.4 (1)
(3.12) $Cr_3^+ \rightarrow Cr_2O^+$	2.4 (9)	34 (1)
(3.13) $Cr_3^+ \rightarrow Cr_2O_2^+$	0.106 (5)	1.50 (6)
(Product in 3.11) $Cr_2^+ \rightarrow Cr^+, CrO^+$	4.1 (3)	58 (5)
(Product in 3.12) $Cr_2O^+ \rightarrow Cr^+$	2.3 (1.3)	33 (18)
(Product in 3.12) $Cr_2O^+ \rightarrow CrO^+$	4.0 (9)	57 (12)
(Product in 3.13) $Cr_2O_2^+ \rightarrow Cr^+, CrO^+$	3.8 (6)	55 (8)

105 ± 5 Å^2 at room temperature, is twice as large as that of Cr_2^+. For both Cr_2^+ and Cr_3^+, Cr^+ was the most dominant product, the difference being in their cross sections for production of CrO^+. As for Cr_2^+, the cross section to produce CrO^+ ($= \sigma_{(2,0 \rightarrow 1,1)}$) was as large as 13.1 ± 0.1 Å^2, while that for Cr_3^+, 3.7 ± 0.8 Å^2 ($= \sigma_{(3,0 \rightarrow 1,1)}$), was much smaller than those of the other two major branches, Cr^+ and Cr_2O^+; the direct production of CrO^+ turned out to be only $\sim 4\%$ of all the reaction paths of Cr_3^+.

The fact that the branching fraction of CrO^+ with respect to Cr^+ increased with the storage time implies that CrO^+ was mostly produced via intermediate products. In fact, the reaction cross sections of an intermediate Cr_2O^+ to generate Cr^+ (= $\sigma''_{(2,1\to1,0)}$) and CrO^+ (= $\sigma''_{(2,1\to1,1)}$) are 33 ± 18 and 57 ± 12 Å^2, respectively, which means that oxidation of Cr_2O^+ produces CrO^+ more than Cr^+. This contrasts to the behavior of Cr_2O^+ in the unimolecular dissociation by excess energy, where the fragments have been reported to be $Cr^+ + CrO$ [28]. The total reaction cross section of the intermediate Cr_2O^+ was 90 ± 22 Å^2 (= $\sigma''_{(2,1\to1,0)} + \sigma''_{(2,1\to1,1)}$). This value agrees with that estimated for the same intermediate produced in the $Cr_2^+ + O_2$ reaction, 86 ± 21 Å^2. This agreement suggests that Cr_2O^+ produced from Cr_2^+ proceeds through the same reaction paths as that produced from Cr_3^+. Based on this fact, one may assume that the values of $k'_{(2,1\to1,0)}$ and $k'_{(2,1\to1,1)}$, which were not determinable for the $Cr_2^+ + O_2$ reaction in 3.4.1, are nearly equal to those for the Cr_3^+ reaction, i.e., $k'_{(2,1\to1,0)} = k''_{(2,1\to1,0)}$ and $k'_{(2,1\to1,1)} = k''_{(2,1\to1,1)}$. This assumption is further confirmed in the following subsection. A similar relation holds for the total cross section of Cr_2^+; it was 60 ± 4 Å^2 for Cr_2^+ as produced in the cluster source, and 58 ± 5 Å^2 for an intermediate Cr_2^+ from Cr_3^+. This suggests that the intermediate was thermalized rapidly in the ion trap filled with He buffer gas.

3.4.3 Reaction mechanism of Cr_2O^+ with O_2

The reaction paths of Cr_2O^+ are illustrated in Figure 3.4c. The reaction cross sections to produce Cr^+ and CrO^+, $\sigma_{(2,1\to1,0)}$ and $\sigma_{(2,1\to1,1)}$, were determined as 26.2 ± 0.3 and 61.9 ± 0.6 Å^2, respectively, at room temperature (Table 3.3). These cross sections agree reasonably with $\sigma''_{(2,1\to1,0)}$ and $\sigma''_{(2,1\to1,1)}$, respectively, derived for the intermediate Cr_2O^+ in the $Cr_3^+ + O_2$ reaction. This fact suggests that the intermediate Cr_2O^+ should follow the same reaction paths as that of the thermal-

ized Cr_2O^+. It further implies that the internally hot intermediate is thermalized promptly before reacting with a second O_2 molecule via collisions with the He buffer gas filled in the ion trap.

Table 3.3: Pseudo-first-order rate constants, k, and the reaction cross sections, σ, of each step of elementary reactions.

Reactant step	k_p / s^{-1}	σ(300 K) / Å^2
$Cr_2O^+ + O_2 \rightarrow Cr^+ + (CrO_2)$	2.53 (3)	26.2 (3)
$Cr_2O^+ + O_2 \rightarrow CrO^+ + (CrO_3)$	5.99 (6)	61.9 (6)

3.5   Summary

The reactions of chromium cluster cations with O_2 were investigated in an ion trap. The rate constants of each reaction step were determined by the measurement of the amounts of the reactants and products as a function of the storage time. Both Cr_2^+ and Cr_3^+ generated Cr^+ and CrO^+ as the final products with a branching fraction of $[Cr^+] : [CrO^+] \approx 3 : 1$. The production mechanism of CrO^+ presented a sharp contrast between Cr_2^+ and Cr_3^+; most of CrO^+ was generated directly from the former reactant, whereas $\sim 80\%$ of CrO^+ was produced via an intermediate Cr_2O^+ from the latter. The reaction rate constants obtained for reaction intermediates (Cr_2^+ and Cr_2O^+) were nearly equal to those for the same chemical species prepared in the cluster source. This fact demonstrates that an ion trap filled with a buffer gas allows gas-phase reactions to take place under a thermalized condition and enables investigation of the thermodynamics of chemical reactions involving free clusters.
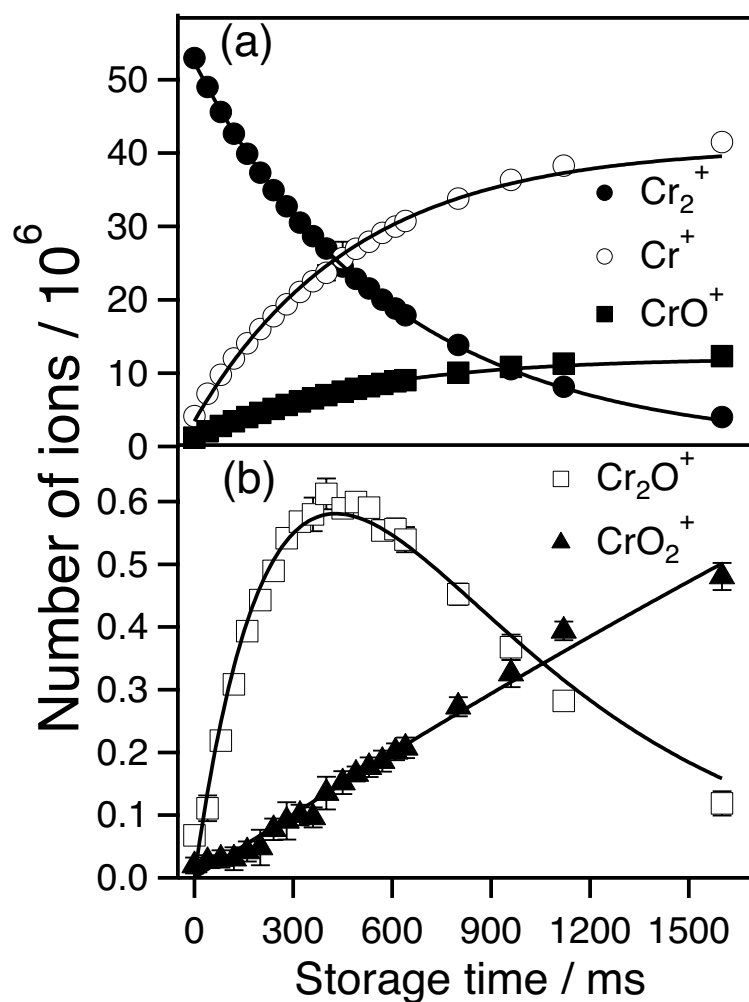
Figure 3.1: Reaction of $Cr_2^+ + O_2$: (a) amounts of the reactant and main products measured as a function of storage time: Cr_2^+ (closed circles), Cr^+ (open circles), and CrOm (closed squares), and (b) minor products displayed in a magnified scale: Cr_2O^+ (open squares) and CrO_2^+ (closed triangles). Fitting curves are superimposed with solid lines.
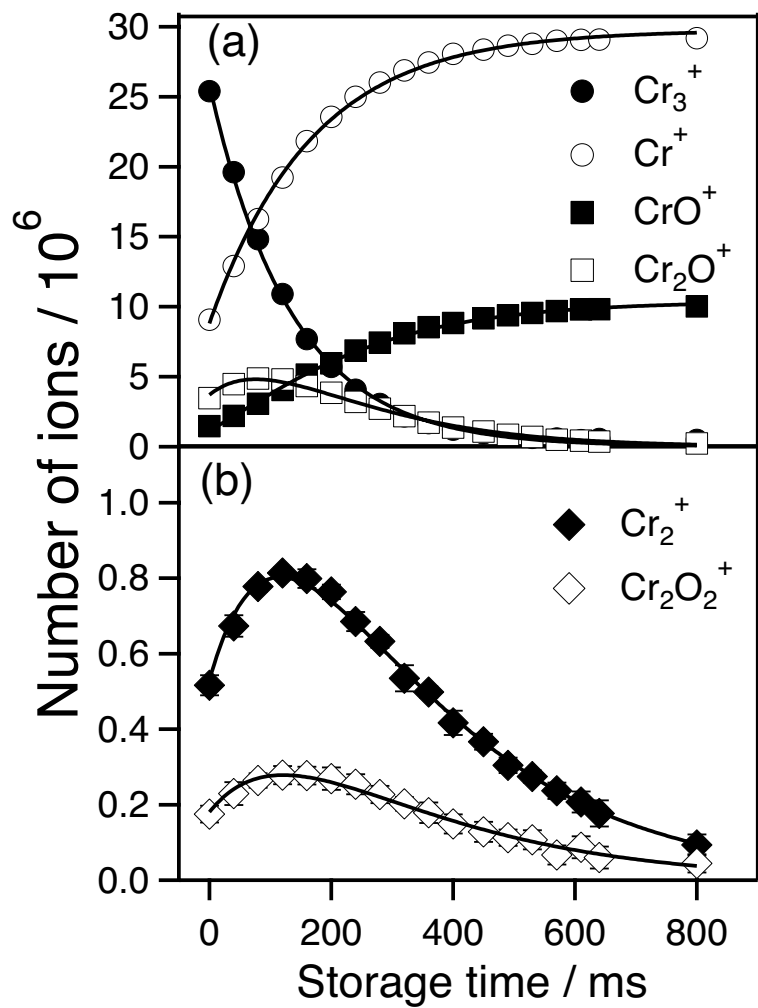
Figure 3.2: Reaction of $Cr_3^+ + O_2$: (a) amounts of the reactant and main products measured as a function of storage time: Cr_3^+ (closed circles), Cr^+ (open circles), CrO^+ (closed squares), and Cr_2O^+ (open squares), and (b) minor products shown in a magnified scale: Cr_2^+ (closed diamonds) and $Cr_2O_2^+$ (open diamonds). Fitting curves are superimposed with solid lines.
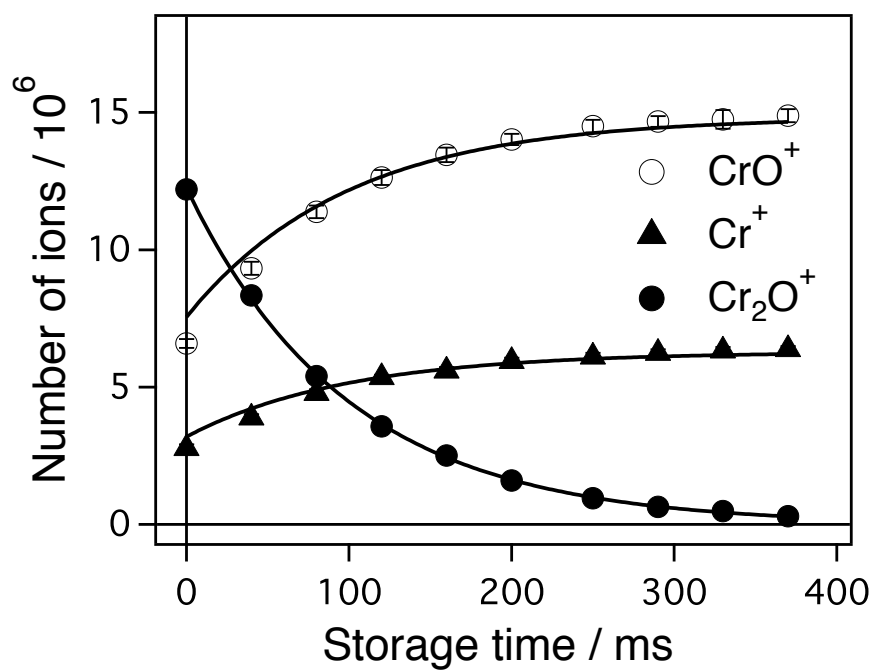
Figure 3.3: Reaction of $Cr_2O^+ + O_2$: Cr_2O^+ (closed circles), Cr^+ (closed triangles), and CrO^+ (open circles). Fitting curves are superimposed with solid lines.
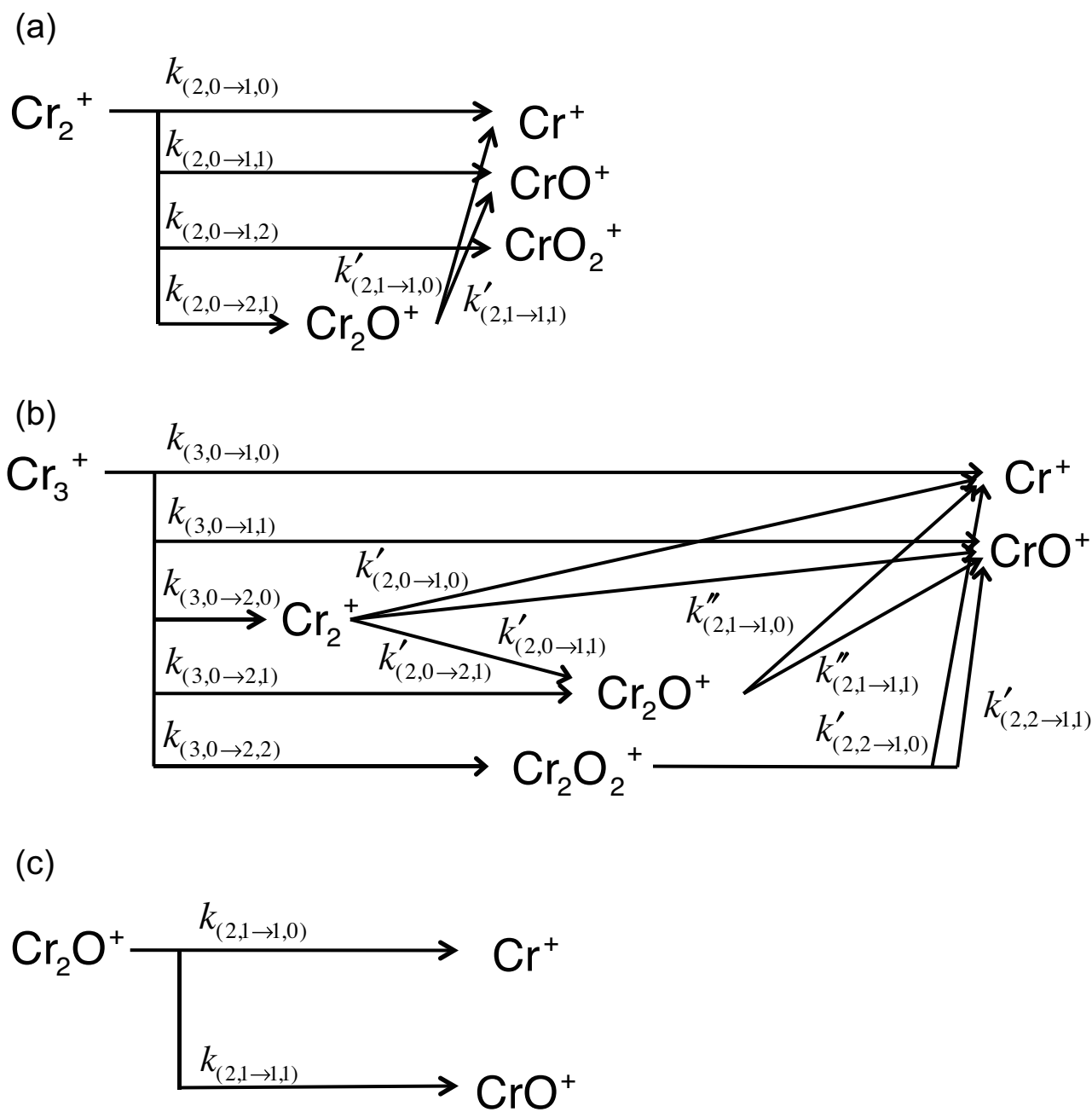
Figure 3.4: Reaction pathways assumed for the three reactants: (a) Cr_2^+, (b) Cr_3^+, and (c) Cr_2O^+. Symbols k, k', and k'' represent the rate constants of each reaction step; see text for the subscripts.

Chapter 4

Sequential Adsorption Kinetics of Dinitrogens on Silver Clusters

4.1 Introduction

Since nano particles were found to be potentially capable of highly efficient catalytic effects [40], investigation of reactivity with a focus on size dependence fascinates researchers. Because clusters, which are smaller than nano particles, show dramatic size-dependent reactivity, they are considered to be attractive catalytic materials for next generation. With recent increasing attempts at catalytic application of clusters, detailed investigation of reaction mechanisms, e.g., revealing an origin of the reaction and reaction sites, can contribute to development in the practical use of clusters. For example, it is reported that the reactions of size-selected Al_n^- with water [41] and formaldehyde [42] are found to proceed efficiently on active sites in the cluster. In order to investigate such reaction sites systematically, knowledge of adsorption processes of non-reactive molecules on clusters is beneficial. In this chapter, adsorption processes of N_2 molecules on small silver cluster cations are presented to demonstrate a survey of reaction sites. Geometrical and electronic structures of Ag_n^+ ($n = 2$–9) were investigated theoretically [43]. Structures of Ag_n^+ ($n < 12$) were also

experimentally determined by ion-mobility experiment combined with theoretical calculations [**?**]. Although the technique is powerful for determination of geometrical structures, it has a difficulty when there are isomers with similar cross sections. Further structural information was obtained by Manard et al. with a temperature-dependent equilibrium method applied for adsorption of C_2H_4 molecules, which are electron donating ligands, on Ag_n^+ ($n = 3$–7) [44]. To eliminate perturbation effects of the ligands in this method, weakly bound ligands, i.e., physisorbing molecules such as nitrogen molecules are favorable because these ligands would not make chemical bonds. Schmidt's group reported a number of studies on reactions of Ag_n^+ with N_2 molecules [45–48]. They show the geometrical structures, the binding energy of N_2, and coadsorption effect on N_2 adsorption caused by pre-adsorbed N_2 based on molecular beam experiment. Here, adsorption processes of N_2 molecules on size-selected silver cluster cations, Ag_n^+ ($n = 1$–10), will be investigated in an ion trap with a focus on reaction kinetics at a given temperature. The temperature of the reaction system was controlled by thermalization processes through collisions with a buffer gas in the trap [46–49].

4.2   Experimental

Experimental setup and procedures used for reaction kinetics measurements have been described in detail in Chapter 2 and elsewhere [30, 50]. Silver clusters were formed from a silver target sputtered by Ar^+ in a magnetron-sputtering cluster-ion source. The cluster cations were stabilized through collisions with He atoms, which was cooled by liquid nitrogen, and were transported by radio-frequency octopole ion guides. The ions were mass-selected by a quadrupole mass filter and introduced into a linear ion trap for 200-ms loading time, where a reactant N_2 gas was introduced

continuously along with a buffer He gas. The end of the loading time was defined as the beginning of the storage time ($t = 0$). After storage of the ions for a given time t, the ions were extracted for mass-analysis by a second quadrupole mass filter, and detected by a current detector. The amounts of the reactant and product ions were recorded as a function of storage time t for the reaction kinetics measurements. The temperature of the ion trap, which was monitored by a carbon resistance thermometer, was cooled down to about 100 K by liquid nitrogen for temperature-dependence measurements.

Theoretical calculations were performed in order to determine which atom of the silver cluster adsorbs a N_2 molecule, i.e., geometrical structures of $Ag_n(N_2)_m^+$. The structural properties and relative energies of these species were calculated by using density functional theory (DFT) with the hybrid B3LYP functional [51,52] and with modified LANL2DZ [53] and cc-pVDZ for Ag atoms and N atoms, respectively, for basis sets. All calculations were performed by the Gaussian09 program [20].

4.3   Results

4.3.1   Adsorption kinetics of N_2 on Ag_n^+

No N_2 adducts on silver cluster cations were detected under room temperature conditions. This inertness of the silver clusters against N_2 suggests that interaction energy between Ag_n^+ and N_2 is smaller than the internal energy of the system at room temperature. By cooling down the ion trap, adsorption of N_2 on Ag_n^+ occurred at ca. 120 K. Since neither reactions nor adsorption were observed at room temperature, the observed adsorption may be physisorption, that is, the bond of the N_2 molecule remains intact in $Ag_nN_2^+$. Figure 4.1 shows a temporal evolution of the intensities

of reactant and product ions in the reaction of Ag_5^+ with N_2 at 105 K. The reactant, Ag_5^+, decreased exponentially with the storage time, and as a result, N_2-adducts, $Ag_5(N_2)^+$ and $Ag_5(N_2)_2^+$, were produced. After 1.5-s storage, the amounts of the reactant and products leveled off; the reaction reached equilibrium with the original reactant left. Since up to two N_2 molecules were adsorbed on the cluster ion, the maximum number of adsorbed N_2, n_{ad}, at 105 K was recorded to be two in this case. The branching ratio of the products in the reaction was dependent on the temperature of the system and the concentration of N_2. The lower the temperature and the higher the concentration, the more the adsorbed N_2 molecules; $Ag_5(N_2)_4^+$ was observed for the Ag_5^+ measured at 95 K.

In the case of Ag_6^+, the reactant ions were completely consumed during the 2-s reaction as shown in Figure 4.2. The adsorption reaction finally reached an equilibrium as in the case of Ag_5^+. The maximum number was determined to be three. This reaction-kinetics measurement was extended to the size range of $n = 1$–10. Kinetics data and maximum numbers thus obtained at 105 K are listed in Table 4.1.

4.3.2   Results of theoretical calculation

Stable geometrical structures of Ag_n^+ were explored by DFT calculations in order not only to confirm structures reported, but also to calculate structures of N_2-adducts to determine the adsorption energy and the adsorption site of N_2 on the Ag_n^+. The low-energy structures of Ag_n^+ obtained are shown in Figure 4.3 with its relative energy in eV. For Ag_5^+ and Ag_7^+, only one possible structure was obtained, other structures reported previously, i.e., 5–II and 5–III in the Figure 4.3, were found to be unstable with an imaginary frequency by the calculations.

Figure 4.4 shows obtained geometrical structures of $Ag_n(N_2)_m^+$ with its adsorption
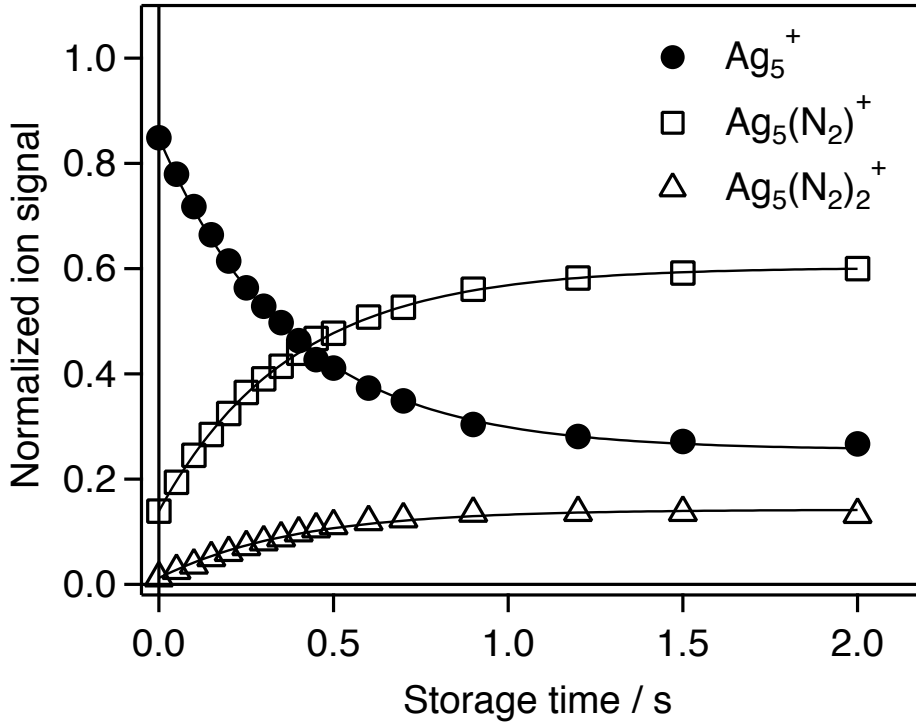
Figure 4.1: Adsorption kinetics of N_2 on Ag_5^+ measured at 105 K. Amounts of the reactant and product ions are plotted as a function of storage time: Ag_5^+ (closed circles), $Ag_5(N_2)^+$ (open squares), and $Ag_5(N_2)_2^+$ (up-pointing open triangles). The partial pressure of N_2 was 0.02 Pa. Solid lines are the fit curves based on rate equations.

energy in eV. Note that the indicated energy is for the first N_2, that is, the production energy of $Ag_n(N_2)^+$ from Ag_n^+ and N_2. It was confirmed that the binding energy was weakened by less than 50 meV when other adsorbed N_2 molecules exist; namely, coadsorption effect, which can be ignored in the present systems.
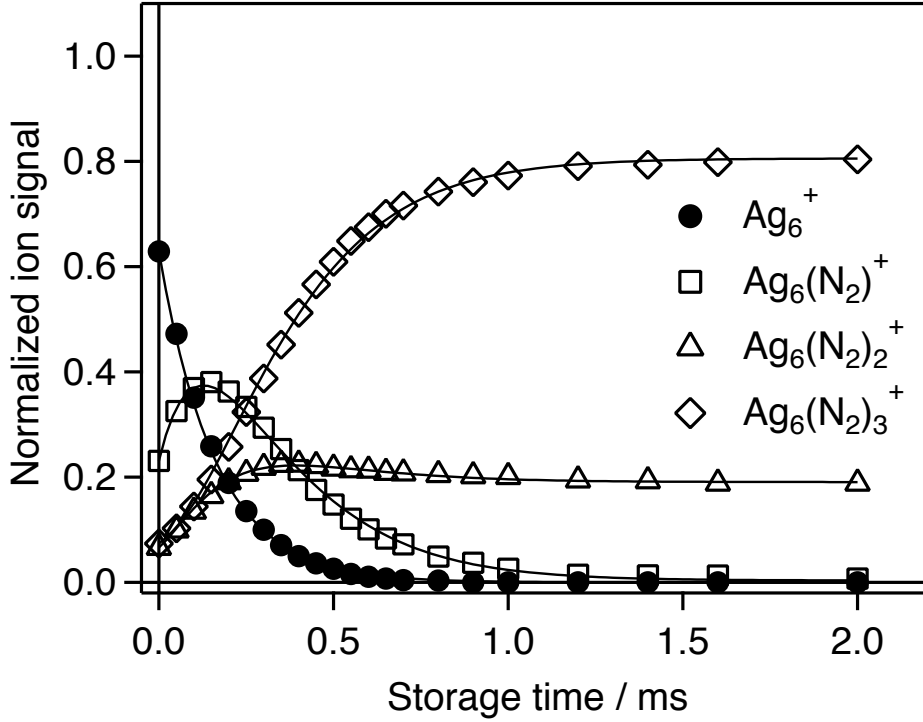
Figure 4.2: Adsorption kinetics of N_2 on Ag_6^+ measured at 105 K. Amounts of the reactant and product ions are plotted as a function of storage time: Ag_6^+ (closed circles), $Ag_6(N_2)^+$ (open squares), $Ag_6(N_2)_2^+$ (up-pointing open triangles), and $Ag_6(N_2)_3^+$ (down-pointing open triangles). The partial pressure of N_2 was 2.7 $\times$ 10^{-3} Pa. Solid lines are the fit curves based on rate equations.

4.4 Discussion

4.4.1 Evaluating an adsorption rate of N_2 and its size dependence

On the basis of temporal evolutions of the intensities of Ag_n^+ and its N_2 adducts, adsorption processes are described by simple sequential adsorption as follows:

$$Ag_n(N_2)_{m-1}^+ + N_2 \quad \rightleftarrows \quad Ag_n(N_2)_m^+. \tag{4.1}$$
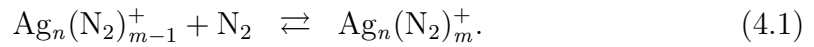
Table 4.1: The maximum number of adsorbed N_2, and the number of equivalent atoms in the most stable silver cluster cations. All the values were measured at 105 K.

Size n	n_{ad}	n_{eq}
1	2	1
2	2	2
3	3	3
4	4	$2+2$
5	2	4
6	3	$2+2+2$
7	2	$2+5$
8	0	
9	0	
10	2	$2+4+4$

In the experimental conditions, the number density of the cluster ions was much lower than that of reactant N_2 and buffer He gas. The N_2 and He were introduced with a constant flow rate so that their partial pressures remained unchanged. Since the densities of the reactant gases were kept as constant throughout reaction-kinetics measurement the present adsorption processes are regarded as pseudo-first-order reactions. Pseudo-first-order adsorption rates for the ions, k_p, were obtained by fitting the data to rate equations using a software called "DETMECH" [54]. In the simple adsorption processes, an energy releasing path by drifting He gas should be considered, i.e., termolecular reactions are applied to kinetics analyses.

$$\mathrm{Ag_n^+ + N_2} \quad \rightleftarrows \quad \left[\mathrm{Ag_n(N_2)^+}\right]^* \tag{4.2}$$

$$\left[\mathrm{Ag_n(N_2)^+}\right]^* + \mathrm{He} \quad \rightarrow \quad \mathrm{Ag_n(N_2)^+ + He^*} \tag{4.3}$$
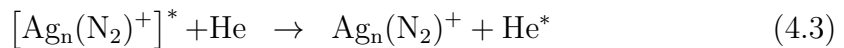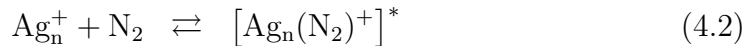
An asterisk in Eq 4.2 stands for an internally hot complex due to the adsorption energy of N_2. Based on these processes, a termolecular adsorption rate of mth N_2, k_m^{III}, is derived as

$$k_m^{III} = k_p / (n_{N_2} \cdot n_{He}) \qquad (4.4)$$

where n_{N_2} and n_{He} represent the densities of the gases in the ion trap. Termolecular rate constants are listed in Table 4.2. Note that the rate constants are subject to a systematic error of 20% because of uncertainty in the partial pressure of N_2. Since the experimental condition was the high-pressure limit of Lindemann mechanism ($k_d[\text{He}] >> k_s$), the termolecular rate coefficients are expressed as follows:

$$k_m^{III} = k_a \cdot k_s / k_d, \qquad (4.5)$$

where k_a is the association rate of N_2, k_s is the stabilization rate by He or N_2, and k_d is the dissociation rate caused by an excess energy upon adsorption. For ion–molecule reactions, k_a and k_s can be estimated by Langevin cross sections. If the effect of geometrical structures of Ag_n^+ is ignored, the apparent adsorption rates should depend only on the rate of the N_2-release path, namely, backward path of Eq 4.2 (k_d), because the interaction rates between ion and gases, k_a and k_s, are constant. The dissociation rates, k_d, can be estimated by referring to Rice–Ramsperger–Kassel (RRK) theory as follows:

$$k_d = \nu \left\{ \frac{E_{int} - D}{E_{int}} \right\}^{3(n+2)-5}, \qquad (4.6)$$

where ν is the vibration pre-factor, E_{int} is the internal energy including an adsorption energy of N_2, D is the dissociation energy of N_2, and n is number of silver atoms in the system.

Figure 4.5 shows adsorption rates of the first N_2 molecule on Ag_n^+ as a function of cluster size. The measured rate increased exponentially with size, although no N_2 molecules were adsorbed on Ag_8^+ and Ag_9^+. The adsorption rate calculated on the basis of Eq 4.5 and Eq 4.6 shows similar size-dependence because of the increased in the degrees of freedom of the system. The exponential increase in the adsorption rate of the first N_2 with size was, therefore, concluded to be due to reduced dissociation rates in larger sizes with larger number of the internal degrees of freedom. In other words, the adsorption rates of N_2 on Ag_n^+ are dominated by statistical rates of redistribution of an adsorption energy.

Table 4.2: Termolecular rates of N_2 adsorption on Ag_n^+ measured at 105 K. k_m^{III} indicates the adsoption rate of the mth N_2 molecule on $Ag_n N_{m-1}^+$.

Size n	k_1^{III} / cm^6 s^{-1}	k_2^{III} / cm^6 s^{-1}	k_3^{III} / cm^6 s^{-1}
1	4.3×10^{-30}	3.8×10^{-28}	
2	2.2×10^{-29}	7.5×10^{-28}	
3	2.2×10^{-29}	3.5×10^{-28}	3.7×10^{-28}
4	(1.8×10^{-28})		
5	4.6×10^{-28}	9.2×10^{-28}	
6	1.2×10^{-26}	1.1×10^{-26}	1.7×10^{-26}
7	1.2×10^{-26}	1.4×10^{-26}	
8			
9			
10	3.1×10^{-28}	6.0×10^{-28}	

4.4.2 Geometrical structure of $Ag_n N_2^+$

$\boldsymbol{n = 3}$. Since n_{eq} in the most stable structure is three as shown in Figure 4.3, it is expected that n_{ad} of Ag_3^+ be three as well. This is consistent with the experimental result. The experimentally determined n_{ad} was three. The agreement of n_{ad} and n_{eq}

suggests that at least a part of Ag_3^+ exists as a triangle shape. In addition to n_{ad} and n_{eq}, termolecular rate constants of the second and the third N_2, k_2^{III} and k_3^{III}, are approximately equal to each other, which proposes that the second and the third N_2 are adsorbed on the equivalent sites. Therefore, one can rule out the possibility of existence of a metastable isomer, namely, a linear isomer of Ag_3^+.

$\boldsymbol{n = 4}$. Since both n_{ad} and n_{eq} are four, the geometrical structure of Ag_4^+ is presumed to be a rhombus, which is the most stable structure from theoretical calculation. It was confirmed that Ag_4^+ easily dissociates to form Ag_3^+ during injection into the ion trap as reported previously. The dissociation resulted in 7 reaction products, $Ag_4(N_2)_{1-4}^+$ and $Ag_3(N_2)_{1-3}^+$. Therefore, it was impossible to determine termolecular rate constants of the reaction of Ag_4^+ with N_2 because of low quality of fitting. The existence of Y-shaped Ag_4^+ cannot be completely excluded.

$\boldsymbol{n = 7}$ **and** $\boldsymbol{10}$. The n_{ad} and n_{eq} agreed with each other in the cases of $n = 7$ and 10 as well. For Ag_7^+, the only single isomer was found from calculations, which is shown in Figure 4.3. Unfortunately, owing to the fact that the number of the equivalent sites of both the most and the second most stable isomers of Ag_{10}^+ was two, further discussion on the structure cannot be made despite of the correspondence of n_{ad} and n_{eq}.

$\boldsymbol{n = 5, 6, 8,}$ **and** $\boldsymbol{9}$. However, n_{ad} and n_{eq} disagree for $n = 5, 6, 8,$ and 9. The reasons for this disagreement can be explained by consideration of reaction kinetics and calculated adsorption energies of N_2. Since both the reactions of Ag_5^+ and Ag_6^+ reached an equilibrium in the experiment, adsorbed N_2 molecules were liberated by the internal energy of the system because the N_2 molecules are weakly bound . The most stable Ag_5^+ has four equivalent atoms. However, the products observed upon equilibrium were not fully adsorbed; $Ag_5(N_2)^+$, $Ag_5(N_2)_2^+$, and even Ag_5^+ were observed. Existence of these products means that release of adsorbed N_2 occurs

before production of a saturated ion, $Ag_5(N_2)_4{}^+$, during sequential adsorption of N_2. By referring to the binding energy of N_2 from calculations, that of Ag_5^+ (< 0.4 eV) is lower than those of the other sizes. Therefore, the disagreement of n_{ad} and n_{eq} is ascribed due to weakly bound N_2 on Ag_5^+.

The reason for the formation of unsaturated products, $Ag_6(N_2)_3{}^+$, is also understood as in the case of Ag_5^+. The fact that two products, $Ag_6(N_2)_2{}^+$ and $Ag_6(N_2)_3{}^+$ were obtained on the equilibrium condition means only the third N_2 repeated an adsorption-dissociation cycle. Ag_6^+ has three different pairs of equivalent atoms; the binding energies on each site are calculated to be 0.45 and 0.28 eV for sites (A) and (B), respectively, whereas no stable structures of $Ag_6(N_2)^+$ were found for N_2 adsorption on site (C). The first two N_2 are bound on Ag (A) and not expected to dissociate throughout storage time, while the third N_2 may be weakly adsorbed on Ag (B). Therefore, it is conceivable that the equilibrium condition between $Ag_6(N_2)_2{}^+$ and $Ag_6(N_2)_3{}^+$ was caused by attaching and releasing a N_2 molecule on the atom (B), which resulted in the disagreement of n_{ad} and n_{eq}.

No binding of N_2 on Ag_8^+ and Ag_9^+ suggest that the interaction energy between the cluster ions and N_2 be too low to maintain the bond. The adsorption, caused by ion–induced dipole interaction in this case, is weakened by dilution of the cationic charge $+e$ into constituent atoms in the cluster and by increase in the distance from N_2 to the charge center; both the effects become more significant for larger sizes of Ag_n^+. Additionally, metal atoms with a low-coordination number are reported to physisorb rare gas atoms more strongly [55]. Therefore, the binding energy may decrease with the cluster size. The largest stabilization energy to form $Ag_n(N_2)^+$ from Ag_8^+, Ag_9^+, and Ag_{10}^+ were calculated to be 0.30 eV, 0.28 eV, and 0.24 eV, respectively, which are lower than those of the Ag_{1-7}^+. These binding energies may not be sufficient to maintain adsorption bonds at 105 K. At the present stage, the

reason for $Ag_{10}(N_2)^+$ formation is not clear.

4.5 Summary

The adsorption processes of dinitrogens on silver cluster cations, Ag_n^+ ($n = 1$–10), were investigated under the multiple-collision conditions using a temperature-controlled ion trap. All the clusters except for Ag_8^+ and Ag_9^+ adsorbed more than one N_2. The termolecular rate constants of the sequential adsorption step were determined by the kinetics data. The rates of the observed processes were found to be dominated by internal degrees of freedom based on the fact that the rate constant increase exponentially with the number of constituent atoms in the ions. The maximal number of adsorbed N_2 allowed the determination of geometrical structures of Ag_n^+, which were supported by theoretical calculations. The inertness of Ag_8^+ and Ag_9^+ were attributed to weak binding of N_2, which were evaluated by calculations as well. The determination of physorption site of Ag_n^+, as demonstrated in the present study, ensures investigation of reaction mechanisms with other molecules such as CO, because adsorption is the primary step of ion–molecule reactions.

3–I　　3–II, 1.18 eV　　4–I　　4–II, 0.144 eV

5–I　　(5–II)　　(5–III)

6–I　　6–II, 0.176 eV　　7–I　　(7–II)

8–I　　8–II, 25.9 meV　　9–I　　9–II, 13.7 meV

10–I　　10–II, 62.2 meV
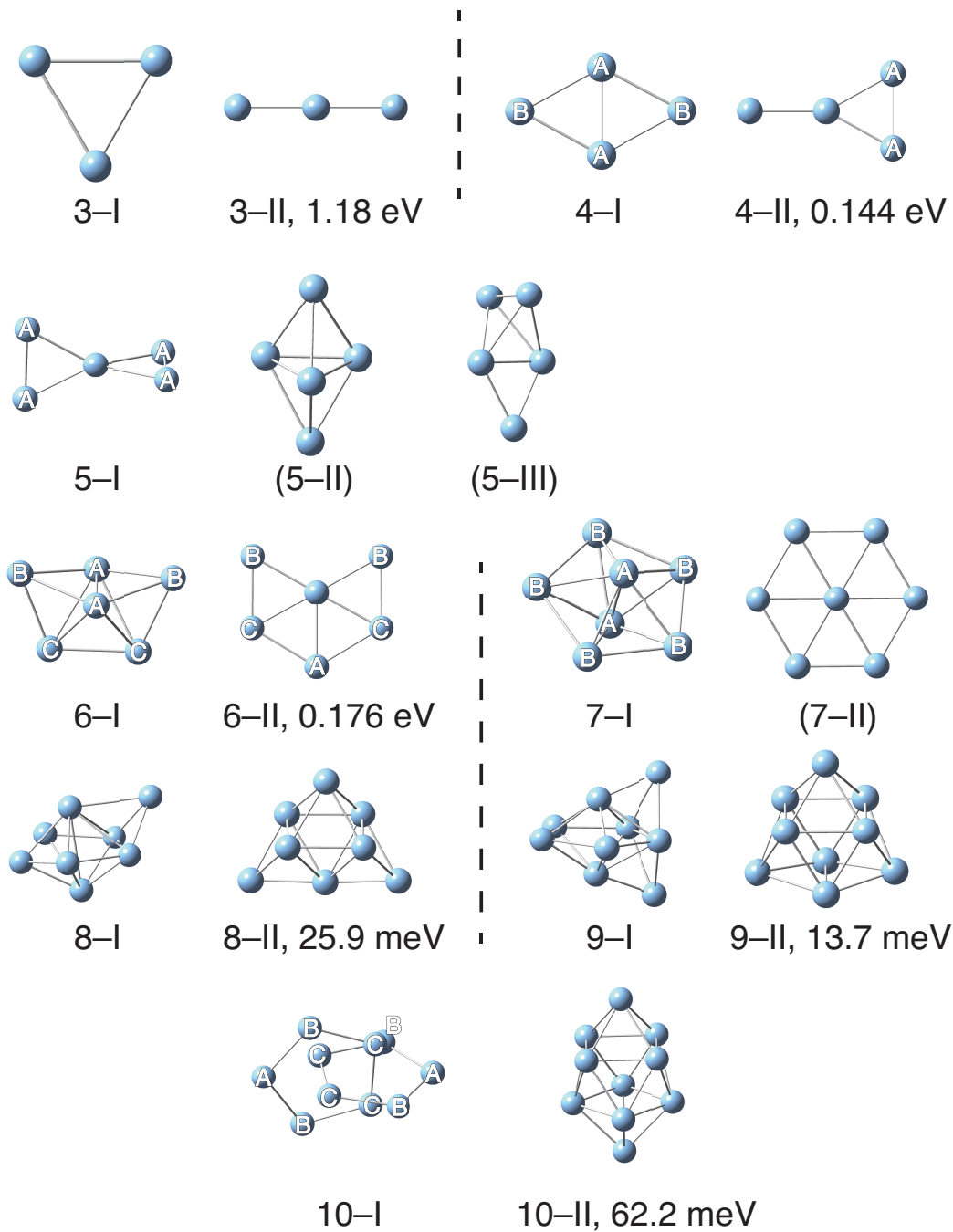
Figure 4.3: Geometrical structures of Ag_n^+ obtained by DFT calculations with B3LYP/modified LANL2DZ level.
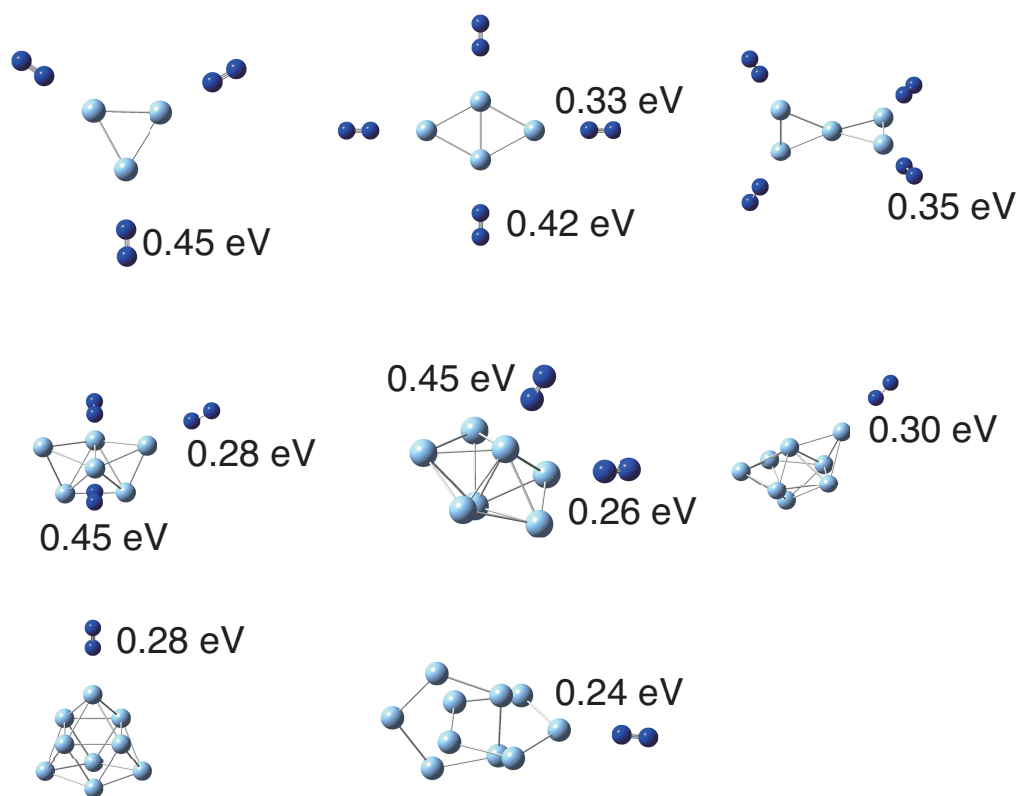
Figure 4.4: Geometrical structures of $Ag_n(N_2)_m^+$ and binding energies of N_2 obtained by DFT calculations.
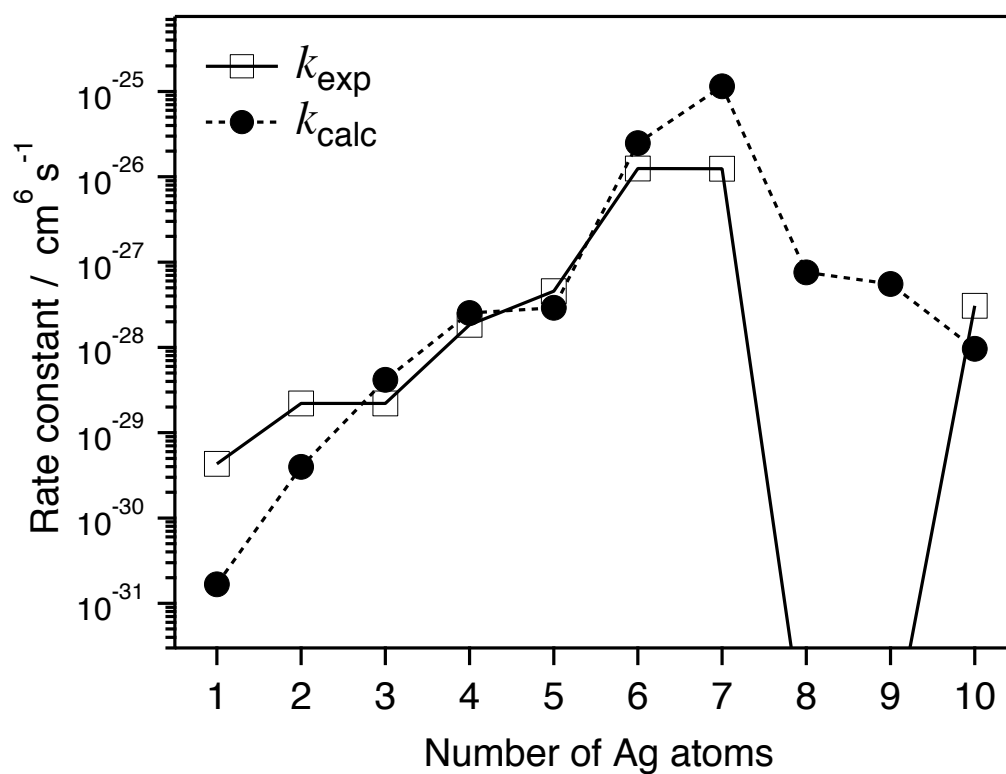
Figure 4.5: Termolecular rate constants of the first N_2 adsorbing on Ag_n^+ as a function of size n. Closed circles represents experimental determined values, and closed squares represents calculated values using Langevin rates and RRK theorem.

Chapter 5

Reactivity of the Gold Dimer Cation Induced by Coadsorbed Molecules

5.1 Introduction

Ever since the catalytic activity of gold nanoparticles on metal-oxide supports were discovered [56], there has been explosive growth, in the number of investigations and consequent reports in the literature, on the ability of gold nanoparticles, both supported and unsupported, to catalyze a very wide range of reactions [57, 58]. Among these reactions oxidation of CO is considered as a benchmark reaction to evaluate the catalytic activity, since its mechanism is well understood. Large number of reports have confirmed that the catalytic activity not only depends on the size of the nanoparticle but also the support, which influences the oxidation states of metals in nanoparticles [59, 60]. It can be envisaged that the reactivity of metal nanoparticles can be modulated by the size and also the nature of the support. It has been shown that reducing metal oxides (such as TiO_2) have much better catalytic activity in comparison to non-reducing metal oxide supports (such as Al_2O_3) [61, 62]. The extreme view in this regard is that metal in zero oxidation states do not

exist on the supported surfaces [63]. The catalytic activity may be controlled more dramatically in the cluster regime by taking an advantage of precise control of the number of constituent atoms. For instance, the low temperature oxidation of CO to CO_2 in the presence of O_2 over gold clusters has size dependence, wherein the clusters of very low diameters (~ 0.5 nm) were found to be most effective catalysts with Au_8 being the smallest catalytically active size [64]. In this regard, investigations of reactions on the small gas phase clusters facilitate understanding the size and consequent electronic effects thereby elucidating the detailed reaction mechanism of catalytic activity. The catalytic properties of size selected metal clusters have been a subject of great interest in many environmentally benign reactions, such as the water gas shift (WGS) reaction,

$$H_2O + CO \rightleftarrows H_2 + CO_2 \tag{5.1}$$

which is well known for the industrial production of clean molecular hydrogen (H_2). The WGS reaction is exothermic, therefore low temperature is desired for better yields. However, low temperature leads to lower reaction rates. The competition between yields and the rates necessitates a suitable catalyst for practical utility. Commercially, the WGS reaction is carried over fine particles of Cu metal dispersed over ZnO/Al_2O_3. Several other metals such as Fe, Ni, Au, Pt, Ru, Ir and others supported on appropriate metal oxides have been used as catalysts for the WGS reaction under varying conditions. In the recent times either FeCr or CuZn particles have been industrially used, which are not suitable for a mobile catalyst because of their pyrophoricity [65]. Due to the ability of gold nanoparticles to catalyze a very wide range of reactions, it can therefore be surmised that a gold based catalyst would be ideal in terms of both reactivity and safer handling. Catalytic activities

of the gold dimer are well examined for CO oxidation by anions [5] and methane activation by cations [66]. DFT calculations on the mechanistic aspects of WGS reaction show that gold dimer cation is a better catalyst in comparison with neutral gold dimer and gold dimer anion [67].

Reactions involving gas phase metal clusters have tremendous utility due to precise control on the size, charge state and, in the case of multi-element clusters, the composition [68]. In the case of CO oxidation over supported gold nanoparticles it has been shown that trace amounts of water in the reactant mixture significantly alters the catalytic activity [69, 70]. This observation can be interpreted as the ability of foreign molecules to control the catalytic activity via the coadsorption effects. Such effects have been reported for CO adsorption on gold-cluster anions in the presence of water vapor [71], for O_2 adsorption on gold-hydroxy cluster anions [72, 73], and on gold-cluster cations with preadsorbed H_2 [74]. In the present work, the ability of pre-adsorbed water molecule to alter the adsorption and reactivity of CO and O_2 on the gold dimer cation is investigated. Reaction kinetics were measured by employing a linear radio-frequency ion trap, where Au_2^+ and CO (or O_2) interacted for a given reaction time. The effect of a water molecule is evaluated by comparing reaction rate constants measured for Au_2^+ and $Au_2(H_2O)^+$.

5.2 Experimental

Details of the experimental apparatus have been described in Chapter 2. Briefly, gold cluster cations were generated in an ion source, where magnetron sputtering of a gold plate is followed by aggregation of sputtered atoms/ions through collisions with helium buffer gas cooled by liquid nitrogen. The cluster ions were guided by radio-frequency octopole ion guides. A pick-up cell was placed downstream of

the cluster ion source for preadsorption of molecules (H_2O, MeOH, or CO) on the gold cluster cations. In the case of water adducts generation, the helium gas was bubbled through water and remixed with pure helium gas to control the composition of water vapor and was introduced into the pick-up cell. The produced ions were mass-selected by a quadrupole mass filter and were stored in a linear octopole ion trap, where a reactant gas (either CO or O_2) was introduced continuously along with a He buffer gas. The ions were stored for a given storage time t, were extracted from the ion trap for mass-analysis by a second quadrupole mass filter, and were detected by a current meter. Partial pressures of the reactant gas and buffer He gas were measured outside the trap by a residual gas analyzer; actual pressures in the trap were evaluated by calibration based on the known reaction explained in Chapter 3. The ion trap and the reactant gases were able to be cooled down to 100 K by liquid nitrogen for low-temperature experiments.

Reaction-kinetics measurement was performed as follows: Mass-selected ions, $Au_2X_m^+$ (X = H_2O, MeOH, or CO, m = 0, 1), were loaded into the trap for 200 ms. The number of ions stored typically reached 1×10^7 within the loading time. The partial pressure of the He buffer gas was adjusted to be in the order of 0.1 Pa throughout the experiment, while the partial pressure of a reactant gas was adjusted to be in the range of 10^{-1}–10^{-5} Pa. The ions stored in the trap were thermalized at the temperature of the He gas within few milliseconds [35], time scale of which is much shorter than the reaction rate ($\sim$10 s^{-1}), i.e., the ions were thermalized before reaction. The amounts of reactant and product ions were measured as a function of storage time t to evaluate reaction kinetics.

5.3 Results

5.3.1 Reaction with CO

Kinetics measurements for Au_2^+ + CO reaction were performed at room temperature. The concentration of CO was kept in the order of 10^{-2} Pa. The amounts of $AuCO^+$ and $Au(CO)_2^+$ produced by the reaction of Au_2^+ with CO under multiple collision conditions as a function of storage time are shown in Figure 5.1. Also shown is the decrease in the reactant Au_2^+ in the same time scale. In the ion trap filled with He buffer gas, it was observed that adsorption of CO leads to dissociation of Au–Au bond in Au_2^+, which is in contrast to a previous report that Au_2^+ does not adsorb any CO molecules in an ion-cyclotron-resonance experiment [75]. The observation of $AuCO^+$ and $Au(CO)_2^+$ indicates the sensitivity of the present experimental techniques, given the fact that the reaction rates and yields for the reactive CO adsorption are very small, *vide infra*.

Figure 5.2 shows temporal evolution of a reaction of the hydrated gold dimer cation, $Au_2(H_2O)^+$, with CO at room temperature. For this reaction the partial pressure of CO was lowered to approximately 10^{-5} Pa, which is about three orders of magnitude lower than the partial pressure used for the reaction of bare Au_2^+. The reactant $Au_2(H_2O)^+$ decreased exponentially with the storage time similarly to observations made for the reaction of bare Au_2^+. The temporal profile of $Au_2(CO)^+$ shows growth followed by decay during the course of the reaction, which indicates that it is a reaction intermediate. On the other hand $Au(H_2O)(CO)^+$ and $Au(CO)_2^+$ show growth over the course of the reaction, which therefore can be considered as final products.

Reaction kinetics of $Au_2(MeOH)^+$ with CO is shown in Figure 5.3. The kinetics of the reaction is similar to that of $Au_2(H_2O)^+$ + CO, i.e., the reaction can be

Figure 5.1: Reaction kinetics of Au_2^+ with CO measured at room temperature. Amounts of the reactant and product ions are plotted as a function of storage time: Au_2^+ (closed circles), $Au(CO)^+$ (up-pointing open triangles), and $Au(CO)_2^+$ (open squares). The partial pressure of CO was 7.2×10^{-3} Pa. Fitting curves are superimposed by solid lines.

described by replacing H_2O with MeOH. The similarity implies that roles of H_2O and MeOH in the reaction were equivalent.

5.3.2   Adsorption of O_2

Bare Au_2^+ did not adsorb O_2 even at temperatures down to 100 K. This is consistent with the previous report [76]. The non-reactive character of Au_2^+ suggests that the interaction energy between O_2 and Au_2^+ should be lower than the thermal energy of the system at 100 K.
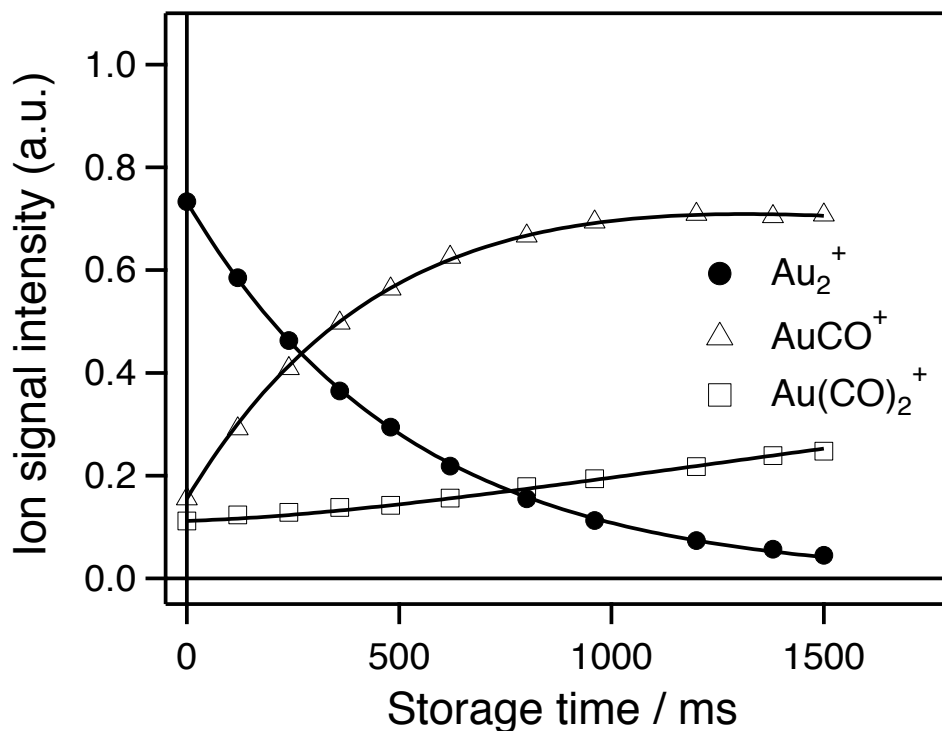
Figure 5.2: Reaction kinetics of $Au_2(H_2O)^+$ with CO measured at room temperature. Amounts of the reactant and product ions are plotted as a function of storage time: $Au_2(H_2O)^+$ (closed circles), $Au_2(CO)^+$ (up-pointing triangles), $Au(CO)_2^+$ (down-pointing open triangles), and $Au(H_2O)(CO)^+$ (open diamonds). The preadsorbed H_2O is denoted as W in the legend. The partial pressure of CO was 1.1×10^{-4} Pa. Fitting curves are superimposed by solid lines.

In striking contrast, a water adduct, $Au_2(H_2O)^+$, exhibited high reactivity against O_2. Figure 5.4 shows reaction kinetics of $Au_2(H_2O)^+$ with O_2 at 100 K, where three product ions, $Au_2(H_2O)(O_2)^+$, $Au_2(H_2O)(O_2)_2^+$, and $Au_2(H_2O)(O_2)(N_2)^+$ were produced. $Au_2(H_2O)(O_2)^+$ was a reaction intermediate, because it disappeared at a long storage time, by adsorbing an additional O_2 molecule leading to the formation of $Au_2(H_2O)(O_2)_2^+$, which is the final product under the present reaction conditions. $Au_2(H_2O)^+$ was able to adsorb up to two O_2 molecules in the reaction time scale of

47
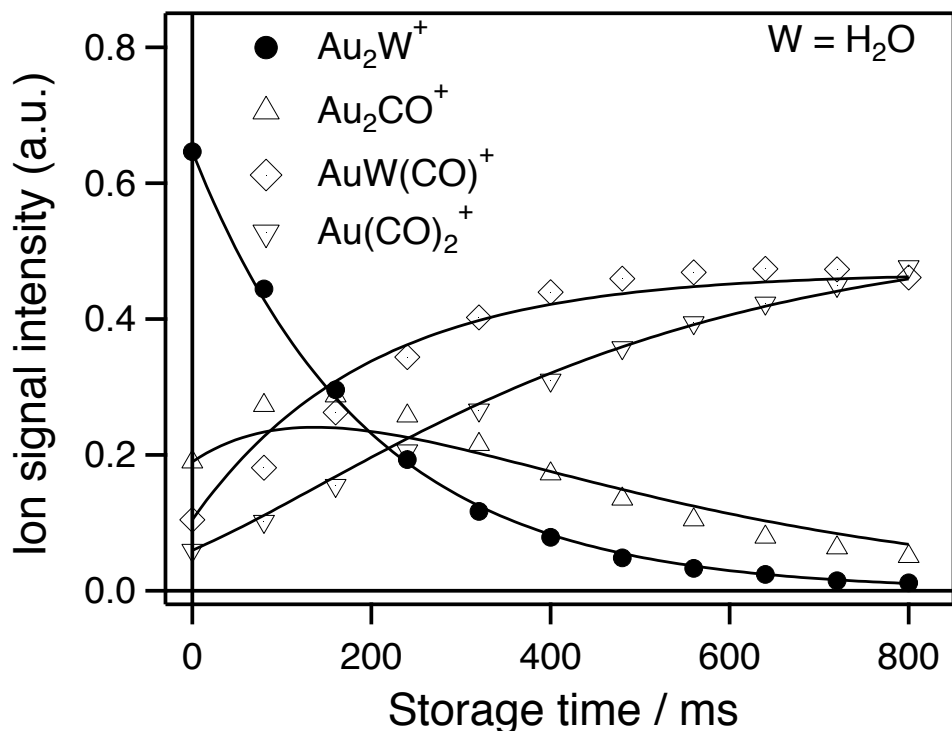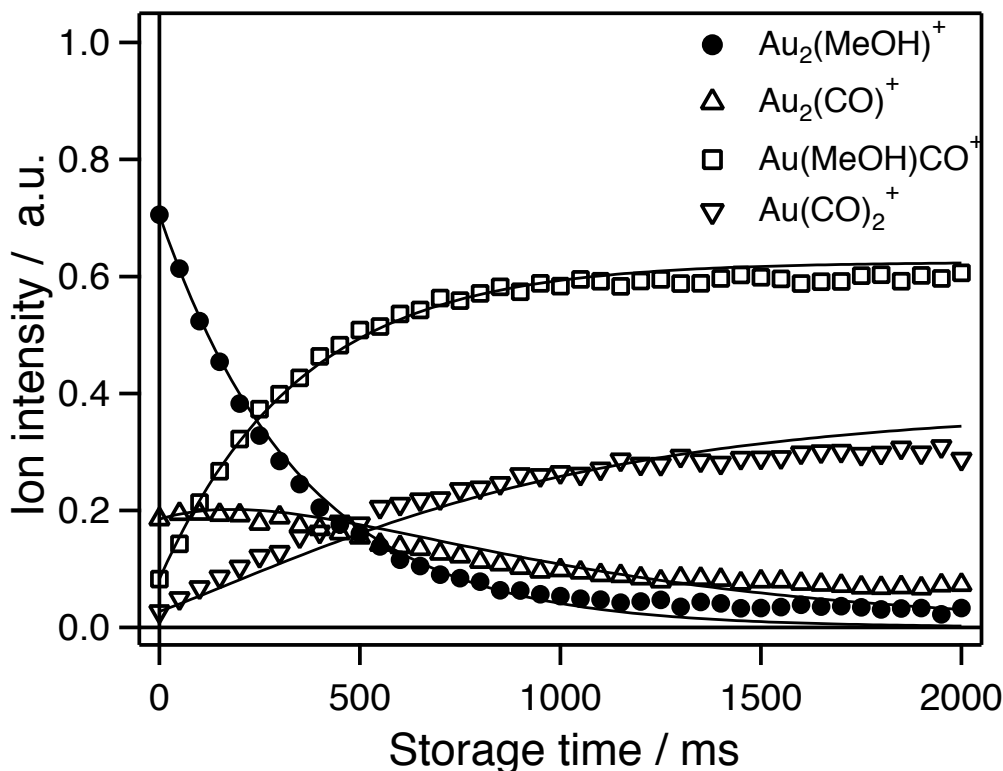
Figure 5.3: Reaction kinetics of $Au_2(MeOH)^+$ with CO measured at room temperature. Amounts of the reactant and product ions are plotted as a function of storage time: $Au_2(MeOH)^+$ (closed circles), $Au_2(CO)^+$ (up-pointing triangles), $Au(CO)_2^+$ (down-pointing triangles), and $Au(MeOH)(CO)^+$ (squares). The partial pressure of CO was 1.5×10^{-5} Pa. Fitting curves are superimposed by solid lines.

about 2 s. Additionally $Au_2(H_2O)(O_2)(N_2)^+$ was observed, which is due to residual N_2 in the ion trap, of which the partial pressure was estimated to be 1.3×10^{-4} Pa.

Reaction of CO-adsorbed Au_2^+ was investigated at 100 K as well, which is shown in Figure 5.5. Similar to the case of the reaction of $Au_2(H_2O)^+$ with O_2, the ions adsorbed up to two O_2 molecules. One adsorbed O_2 enhanced adsorption rate of residual N_2 on the intermediate, $Au_2(CO)(O_2)^+$ as well in the reaction of $Au_2(H_2O)^+$. However, a branching ratio of $Au_2X(O_2)_2^+$ to $Au_2X(O_2)(N_2)^+$ was reversed relative

48

to the case of $Au_2(H_2O)^+$, though the partial pressure of N_2 was 1.1×10^{-4} Pa, which was nearly equal to the condition of $Au_2(H_2O)^+$ reaction.

5.4   Discussion

5.4.1   Evaluation of reaction-rate constants

Reactions rate constants were determined, based on all the observed species from the results of reaction-kinetics measurements depicted in Figures 5.1–5.4, and results are listed in Table 5.1. The methodology for evaluating the rate constants is based on the experimental conditions. The ion trap was maintained at constant partial pressures of He and CO by introducing the gases continuously into the gas cell of the trap. The number density of the CO gas, n_{CO}, was higher than that of the trapped ions at least by three orders of magnitude. Further, the steady state concentration is maintained by continuous flow of CO gas into the gas cell. Therefore, n_{CO} was practically constant over the entire reaction experiments, hence pseudo-first-order reaction. The temporal evolution of the reaction of Au_2^+ with CO shown in Figure 5.1 indicates the following reaction steps:

$$Au_2^+ + CO \quad \rightarrow \quad AuCO^+ + Au \tag{5.2}$$

$$AuCO^+ + CO \quad \rightarrow \quad Au(CO)_2^+ \tag{5.3}$$
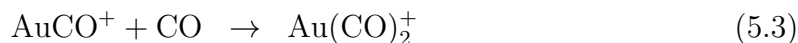
Pseudo-first-order rate constants k_p for the above two pathways were obtained by fitting the data to rate equations with a software "DETMECH" [54]. Based on bimolecular reaction kinetics, an absolute bimolecular rate constant, k^{II}, is derived as $k^{II} = k_p/n_{CO}$. k_p and k^{II} were determined to be 1.91 s^{-1} and 9.4×10^{-13} cm^3 s^{-1}, respectively. Taking into account an ion–induced dipole interaction effect, simple

association rates between ions and molecules can be estimated by the Langevin rate [31], where e is the elementary charge, a is the polarizability of the target gas molecules, μ is a reduced mass of the ion–neutral pair. Since CO has a large permanent dipole moment, the association rate tends to be underestimated only with t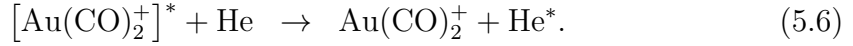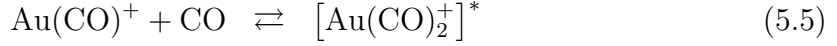he Langevin rate; it is needed to be corrected for ion–dipole interaction by ADO (averaged dipole orientation) theory. The association rate with the ADO theory is expressed as follows [77]:

$$
k_{\text{ADO}} = \left(\frac{2\pi e}{\mu^{1/2}} \right) \frac{1}{4\pi\varepsilon_0} \left\{ \alpha^{1/2} + c\mu_{\text{D}} \left(2/\pi k_{\text{B}}T \right)^{1/2} \right\}. \tag{5.4}
$$

Here, c represents a locking constant ($c = 0.196$ for CO) [78], μ_D is the dipole moment of CO ($= 0.112$ Debye), k_{B} is Boltzmann's constant, and T is the temperature of the system. The association rate of CO was calculated to be 6.6×10^{-10} cm^3 s^{-1}, whereas the experimentally determined reaction rate was 9.4×10^{-13} cm^3 s^{-1}. This means only 0.2% of collisions would indeed lead to CO association. In other words, once a CO molecule interacts with Au$_2^+$, the CO molecule tends to be released in most of the cases. This behavior is understood as follows: A CO molecule is bound to a metal cation more strongly than other ordinary molecules because of electronic back donation from the metal atom to CO. This may create an internally hot intermediate adduct, [Au$_2$(CO)$^+$]*, which proceeds to transition states not only of CO release but also of Au release, i.e., [Au$_2^+\cdots$(CO)]† and [Au(CO)$^+\cdots$Au]†. According to RRKM theory [39], the weakest bond, i.e., the bond between Au$_2^+$ and CO in this case, is to be cleaved preferentially in unimolecular dissociation. The observation of the Au(CO)$^+$ fragment, albeit in very small yields, indicates the sensitivity of the present experimental setup. Formation of Au(CO)$_2^+$, which is due to further CO adsorption on the product of Eq 5.2 as given in Eq 5.3, requires stabilization through

a collision with a He atom of the buffer gas to release excess energy of adsorption.

Formation of $Au(CO)_2^+$ should therefore follow a termolecular mechanism as follows:

$$Au(CO)^+ + CO \; \rightleftarrows \; \left[Au(CO)_2^+\right]^* \tag{5.5}$$

$$\left[Au(CO)_2^+\right]^* + He \; \rightarrow \; Au(CO)_2^+ + He^*. \tag{5.6}$$

According to Eqs 5.5 and 5.6, a termolecular rate constant k^{III} is expressed as $k^{III} = k_p/(n_{CO} \cdot n_{He})$, where n_{CO} and n_{He} represent the densities of the gases in the ion trap. In the present condition, k^{III} was obtained to be 7.8×10^{-28} cm^6 s^{-1}.

Table 5.1: Absolute bimolecular and termolecular rate constants, k^{II} and k^{III}, of each reaction steps. The values are subject to a systematic error of ~20%.

Reaction step	k^{II} / cm^3 s^{-1}	k^{III} / cm^6 s^{-1}
(5.2) $Au_2^+ + CO \rightarrow AuCO^+ + Au$	9.4×10^{-13}	
(5.3) $AuCO^+ + CO \rightarrow Au(CO)_2^+$		7.8×10^{-28}
(5.7) $Au_2(H_2O)^+ + CO \rightarrow Au(H_2O)(CO)^+ + Au$	8.8×10^{-11}	
(5.8) $Au_2(H_2O)^+ + CO \rightarrow Au_2(CO)^+ + H_2O$	1.1×10^{-10}	
(5.9) $Au_2(CO)^+ + CO \rightarrow Au(CO)_2^+ + Au$	1.1×10^{-10}	
(5.10) $Au_2(H_2O)^+ + O_2 \rightarrow Au_2(H_2O)(O_2)^+$		2.0×10^{-25}
(5.11) $Au_2(H_2O)(O_2)^+ + O_2 \rightarrow Au_2(H_2O)(O_2)_2^+$		5.2×10^{-26}
(5.12) $Au_2(H_2O)(O_2)^+ + N_2 \rightarrow Au_2(H_2O)(O_2)(N_2)^+$		1.1×10^{-22}
$Au_2(MeOH)^+ + CO \rightarrow Au(MeOH)(CO)^+ + Au$	1.7×10^{-10}	
$Au_2(MeOH)^+ + CO \rightarrow Au_2(CO)^+ + MeOH$	5.2×10^{-10}	
$Au_2(CO)^+ + CO \rightarrow Au(CO)_2^+ + Au$	1.1×10^{-10}	
$Au_2(CO)^+ + O_2 \rightarrow Au_2(CO)(O_2)^+$		1.6×10^{-25}
$Au_2(CO)(O_2)^+ + O_2 \rightarrow Au_2(CO)(O_2)_2^+$		5.3×10^{-25}
$Au_2(CO)(O_2)^+ + N_2 \rightarrow Au_2(CO)(O_2)(N_2)^+$		3.4×10^{-24}

5.4.2 Coadsorption effect: $Au_2X^+ + CO$

Preadsorption of a H_2O molecule influences the rate constants dramatically. On the basis of the reaction-kinetics measurement in Figure 5.2, reaction pathways of $Au_2(H_2O)^+$ with CO were identified as follows:

$$Au_2(H_2O)^+ + CO \rightarrow Au(H_2O)(CO)^+ + Au \tag{5.7}$$

$$\rightarrow Au_2(CO)^+ + H_2O \tag{5.8}$$

$$Au_2(CO)^+ + CO \rightarrow Au(CO)_2^+ + Au \tag{5.9}$$
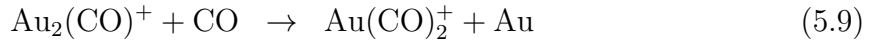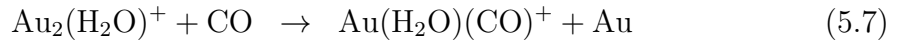
As it mentioned in Subsection 5.3.1, the reaction pathways for $Au_2(MeOH)^+$ can be described by replacing H_2O in Eqs 5.7–5.9 by MeOH. Adsorption of a CO molecule is always accompanied by cleavage of either Au–Au bond or Au–H_2O (Au–MeOH) bond. Bimolecular rate constants were derived for these elementary reactions. The reactivity of $Au_2(H_2O)^+$, i.e., the decay rate of $Au_2(H_2O)^+$, was evaluated to be 2.0 $\times 10^{-10}$ cm^3 s^{-1}. That of $Au_2(MeOH)^+$ was 6.9×10^{-10} cm^3 s^{-1}. These bimolecular rates are much higher than that of Au_2^+ by a factor of 210, or 730. Regarding the rate constants of Au-atom release from Au_2^+ and Au_2X^+, i.e., the rate constants of Eqs 5.2 and 5.7, the latter was about 90 times higher than the former. This provides clear evidence of a weakened Au–Au bond due to adsorption of a H_2O molecule. Binding energies of Au_2^+ and Au_2 have been evaluated to be 2.4 and 2.3 eV [79], respectively, by collision-induced dissociation experiment. In addition, DFT calculation has derived binding energies of Au_2 and Au_2^- to be 2.22 and 1.81 eV [80], respectively. These results imply that the higher the electron density on the gold dimer is charged, the weaker the Au–Au bond. It can therefore be inferred that adsorption of H_2O not only aids in redistribution of adsorption energy of CO [71] but

also leads to partial charge transfer to Au_2^+, thereby increasing the electron density on the gold dimer, which leads to weakening of the Au–Au bond. This results in increase in CO adsorption on Au_2^+ through an adsorption channel accompanied by Au–Au bond splitting as well as liberation of the preadsorbed H_2O.

Although MeOH has lower capability to donate partial electron than H_2O, the effect of weakening the Au–Au bond by MeOH was considered to be comparable to H_2O by inferring from the Au-releasing rates. However, the ligand exchange rate of $Au_2(MeOH)^+$ was higher than that of $Au_2(H_2O)^+$ by five times. This was resulted from weaker bond of Au_2^+–MeOH than that of Au_2^+–H_2O, i.e., the adsorbed MeOH was easily released than the adsorbed H_2O by the adsorption energy of CO.

5.4.3 Coadsorption effect: $Au_2X^+ + O_2$

Adsorption of O_2 on $Au_2(H_2O)^+$ was observed through formation of $Au_2(H_2O)(O_2)^+$ and $Au_2(H_2O)(O_2)_2^+$ as shown in Figure 5.4. The temporal evolution of intensities of ions revealed the following processes:

$$Au_2(H_2O)^+ + O_2 \rightarrow Au_2(H_2O)(O_2)^+ \qquad (5.10)$$

$$Au_2(H_2O)(O)_2^+ + O_2 \rightarrow Au_2(H_2O)(O_2)_2^+ \qquad (5.11)$$

$$Au_2(H_2O)(O)_2^+ + N_2 \rightarrow Au_2(H_2O)(O_2)(N_2)^+ \qquad (5.12)$$
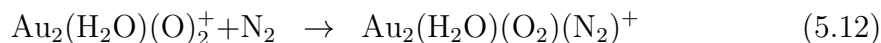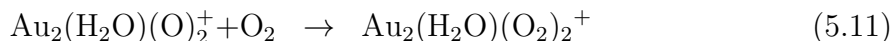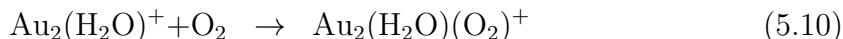
In the case of the reaction of $Au_2(CO)^+$, reaction pathways can be represented by replacing H_2O with CO in Eqs 5.10–5.12 as mentioned in Subsection 5.3.2, although the branching ratio of the final products was reversed. Bare Au_2^+ is completely inert towards O_2 molecule, which has been reported earlier [76]. On the other hand, preadsorption of H_2O molecule facilitates adsorption of O_2 on Au_2^+. Here $Au_2(H_2O)(O_2)^+$ was an intermediate product, which can further adsorb one more

O$_2$ or N$_2$ molecule. The adsorption of O$_2$ on Au$_2$X$^+$ can be due to (a) increases in the number of degrees of freedom of the system, which increase the lifetime of the internally hot complex, and/or (b) partial electron transfer from H$_2$O or CO to O$_2$. The effect of increase in the number of degrees of freedom can be discarded, since it is known that even larger gold cluster cations do not adsorb O$_2$, with an exception of Au$_{10}^+$. However, it is well known that gold cluster anions with even-numbered atoms (odd-electron systems) adsorb O$_2$, which is stabilized by electron donation from the anion to the O$_2$ molecule [76]. It has been recently reported that even neutral gold clusters adsorb O$_2$, which once again are stabilized by electron donation from gold cluster to the O$_2$ molecule, similar to the gold cluster anions [81]. It can therefore be inferred that adsorption of O$_2$ requires electron density on the gold cluster, which is depleted in the cluster cations. However, adsorption of H$_2$O or CO on Au$_2^+$ increases the electron density, relative to bare Au$_2^+$, thereby increasing its propensity for O$_2$ adsorption. The charge modulation observed here is similar to those reported for Au$_n$OH$^-$ clusters [72] and for Au$_n$H$_2^+$ clusters [74].

The adsorption pathways of the second O$_2$ and N$_2$ of in the residual gas are competing processes. The adsorption of N$_2$ was induced because of increase in degrees of freedom of the ions, which is discussed in Chapter 4. Adsorbing two O$_2$ molecules on Au$_2^+$ induced by the coadsorption effects seems to be implausible phenomena under the assumption of partial electron donation from the gold atoms to O$_2$. However, when the preadsorption molecule was CO, the termolecular rate of adsorption of the second O$_2$ was higher than that of H$_2$O. This is reasonable because CO can donate electrons more effectively than H$_2$O, which results in forming more stable two-O$_2$ adsorbed adducts. Therefore the adsorption of the second O$_2$ can be attributed to induction by the preadsorbed molecule as well as the adsorption of the first O$_2$.

5.5 Summary

This chapter presented reaction kinetics of Au_2^+ with CO and O_2 with focuses on coadsorption effect of H_2O and MeOH on the reaction with CO and H_2O and CO on the reaction with O_2. Au_2^+ was found to be almost unreactive with CO and completely inert with O_2. Preadsorption of H_2O and MeOH molecule on Au_2^+ leads to enhanced (by a factor of 210 or 730) adsorption of CO due to the increased rate of Au–Au bond cleavage as well as the release of the preadsorption molecule to liberate the excess internal energy; the former can be attributed to the weakened Au–Au bond following adsorption of the preadsorbed molecule. Preadsorption of H_2O or CO molecule on Au_2^+ initiates adsorption of up to two O_2 molecules. This enhancement and initiation of the reactions by the coadsorbed H_2O (or CO) were attributed to partial electron transfer from the O atom in H_2O (or C atom in CO) to Au_2^+.
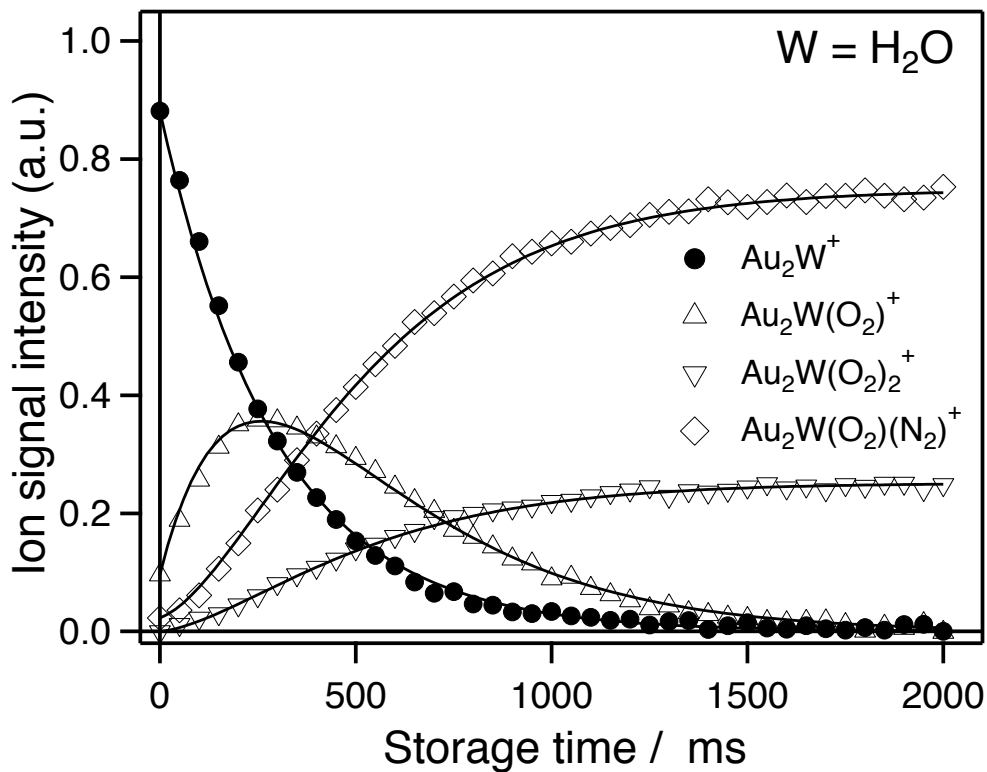
Figure 5.4: Reaction kinetics of $Au_2(H_2O)^+$ with O_2 measured at 100 K. Amounts of the reactant and product ions are plotted as a function of storage time: $Au_2(H_2O)^+$ (closed circles), $Au_2(H_2O)(O_2)^+$ (up-pointing triangles), $Au_2(H_2O)(O_2)_2^+$ (down-pointing open triangles), and $Au_2(H_2O)(O_2)(N_2)^+$ (open diamonds). The partial pressure of O_2 was 9.1×10^{-2} Pa. $Au_2(H_2O)(O_2)(N_2)^+$ was produced due to residual N_2 in the trap. Solid lines are the fits to data according to the reaction kinetics.
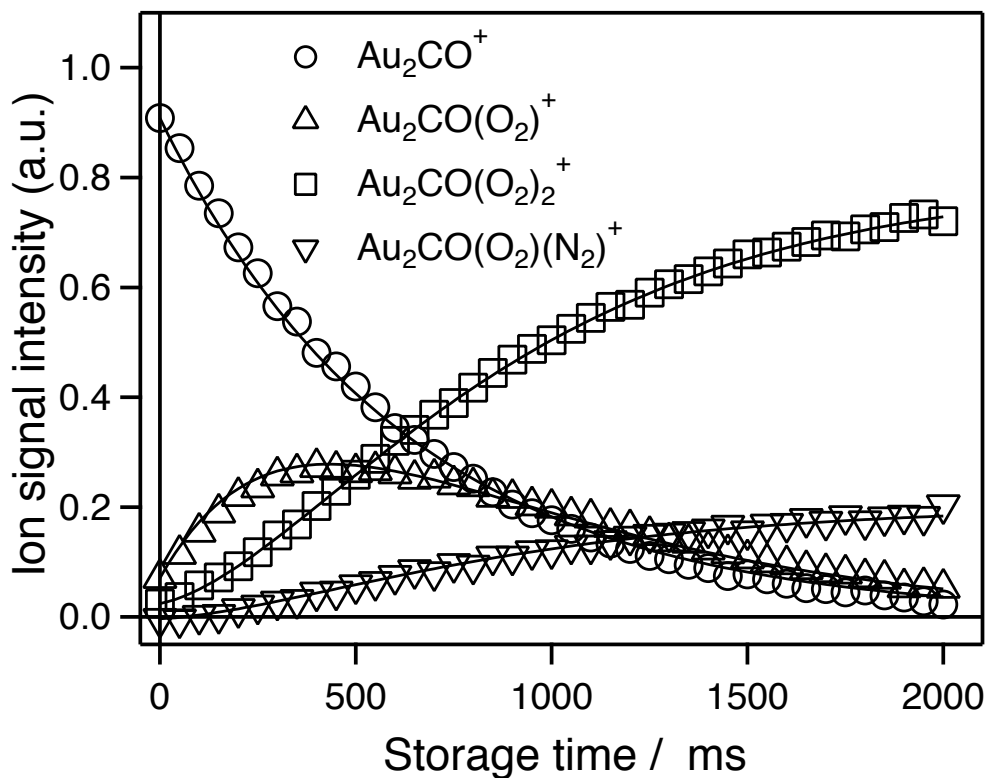
Figure 5.5: Reaction kinetics of $Au_2(CO)^+$ with O_2 measured at 100 K. Amounts of the reactant and product ions are plotted as a function of storage time: $Au_2(CO)^+$ (closed circles), $Au_2(CO)(O_2)^+$ (up-pointing triangles), $Au_2(CO)(O_2)_2^+$ (down-pointing triangles), and $Au_2(CO)(O_2)(N_2)^+$ (open diamonds). The partial pressure of O_2 was 5.4×10^{-2} Pa. $Au_2(H_2O)(O_2)(N_2)^+$ was produced due to residual N_2 in the trap. Solid lines are the fits to data according to the reaction kinetics.

Chapter 6

Optical Absorption Spectroscopy of Silver Cluster Cations

6.1   Introduction

An optical property of a metal is known to vary dramatically with its size. For example, nanoparticles of a metal show intense photoabsorption bands caused by collective excitation of electrons [82,83], whereas corresponding atoms exhibit sharp spectral lines resulting from transitions between atomic orbitals. It is reported by experimental studies that the resonance energy, the intensity, and the width of the resonance peak of a metal nanoparticle depend on the size, the shape, and the dielectric constant of a supporting medium [84–89]. These features of optical resonance in a small metal particle are well described by classical electrodynamics [90], which explains the dependence on the above material parameters. Investigation of optical absorption of metal clusters in the small size range will provide an opportunity for a systematic study of emergence of the collective behavior of electrons, i.e., plasmon-like excitation. Theoretically, evolution of spectra, i.e., from an electronic transition between quantum states to molecular-like and further to plasmon-like, were demonstrated by TD-DFT calculations [91]. Nanoparticles of alkali metals (Na etc.) and

coinage metals (Cu, Ag, and Au) show a broad absorption band in the visible region. Among these metal particles, sodium and copper are difficult to handle in practical applications as they are oxidized easily. The absorption coefficients of the gold clusters, Au_n ($n = $ 2–14 and 20), are reported to be smaller than those of the silver clusters because of the screening effect by d electrons [92]. Therefore, the author focused on silver clusters to investigate the optical properties presented in this chapter. The optical absorption spectra of silver clusters were first measured in a mass-selected cationic cluster beam by the photodepletion method [11, 12]. The absorption spectra were also obtained in rare-gas matrices [9, 93], which were red-shifted due to an interaction with the matrices. The optical absorption has been explored further for the silver clusters bound to tryptophan [94–96] and thiolate [97] for bio-sensing studies because of high biological compatibility of silver. An ion trap is a powerful tool here again for temperature-dependence studies of the optical properties of free cluster ions, as described in the former chapters. Among silver clusters, Ag_9^+ has been studied by many researchers [11, 12, 50, 95] because it is an eight-valence-electron system, i.e., a model of a closed-shell electronic structure. It is known that d electrons play an important role in optical transitions of Ag_{11} [98], whereas transitions in smaller clusters ($n = $ 2–8) are associated mainly with s electrons [99]. This chapter reports photoabsorption spectroscopy of size-selected silver clusters, Ag_n^+ ($n = $ 8–35), in the ultraviolet region (3.7–4.4 eV) for investigation of changes in the optical spectra with cluster growth.

6.2   Experimental and Computational

The experimental apparatus is described in detail in Chapter 2. Silver clusters were generated by a magnetron-sputtering ion source, and size-selected by a quadrupole

mass filter. Size-selected clusters were stored in a 40-cm ion trap, which was filled with a buffer He gas. The pressure inside the ion trap was estimated to be about 10^{-1} Pa. After 0.5-s thermalization in the trap, the cluster ions were irradiated with UV ns laser pulses for 1 s at a repetition rate of 10 Hz. Clusters were stored further for 0.5 s after laser irradiation to ensure dissociation, extracted from the trap, and mass analyzed by a second quadrupole mass filter. Photoabsorption was evaluated as decrease in the parent ions (photodepletion) by laser irradiation because several photofragments were observed with branching fractions dependent on the excitation photon energy. Depletion of the parent ions was evaluated by taking difference between numbers of trapped parent ions with and without irradiation. These on-off measurements were repeated by changing the laser wavelength at an interval of 0.5 nm to obtain an action spectrum of photodissociation. Every data points are obtained by averaging over 20 measurements.

As for the light source, a frequency doubled dye laser (Scanmate 2E, Lambda Physik) pumped by a XeCl excimer laser (COMPex, Lambda Physik) was employed. Three dyes (Rhodamine- 590 chloride, 610 chloride, and 640 perchlorate (Exciton)) covered 285–335 nm (3.70–4.35 eV) with typical pulse energies of about 200 μJ. The intensity of the irradiated laser was monitored at the most downstream by a power meter (Thermal Sensor 3A-P, Ophir) in order to calculate the number of incident photons, n_{photon}. The incident-light power was monitored by a photodiode as well, which was necessary, in particular, to measure an intensity of the light below the detection limit of the power meter (60 μW); calibration was done between the power meter and the photodiode.

Theoretical calculations were carried out for peak assignment. Three calculation levels were adopted, namely, B3LYP/modified LANL2DZ, LC-ωPBE/Def2-TZVP, and CAM-B3LYP/Def2-TZVP because these levels were reported to describe pho-

60

toabsorption spectra of small silver cluster well [16, 17]. All the calculations were performed using Gaussian 09.

6.3 Results

6.3.1 Dissociation process

Photofragmentation resulted from laser irradiation was analyzed by mass spectrometry. Several fragments were observed upon photodissociation of Ag_9^+ as shown in Figure 6.1. The decrease in the amount of Ag_8^+ in the range of 290–294 nm, which was accompanied by generation of Ag_5^+ and Ag_3^+, was due to sequential photodissociation caused by intense incident laser. Therefore, the photo-dissociation pathway of Ag_9^+ in the UV region was considered to be monomer- or dimer- loss as previously reported [100].
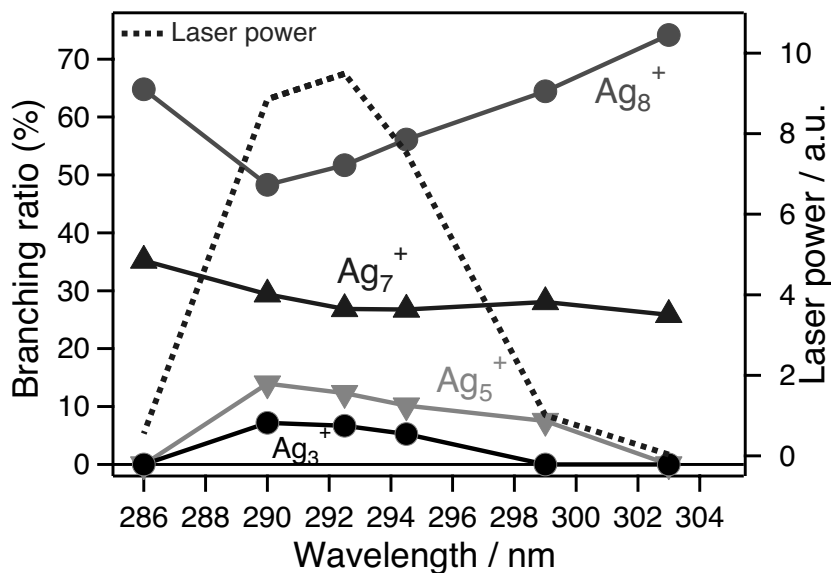
Figure 6.1: Branching fractions of photofragments from Ag_9^+ (left axis) and incident laser power (dashed line, right axis) plotted as a function of wavelength.

61

Figure 6.2 shows photofragment yields of Ag_n^+ ($n = 14$–35) measured at 310 nm (4.0 eV) as a function of incident laser power. The slope of the logarithmic plot of fragment yields vs. laser power was one for n $\leq$ 14, whereas it was two for n $\geq$ 15. This implies that photodissociation of the clusters larger than 15 is a multi-photon process.
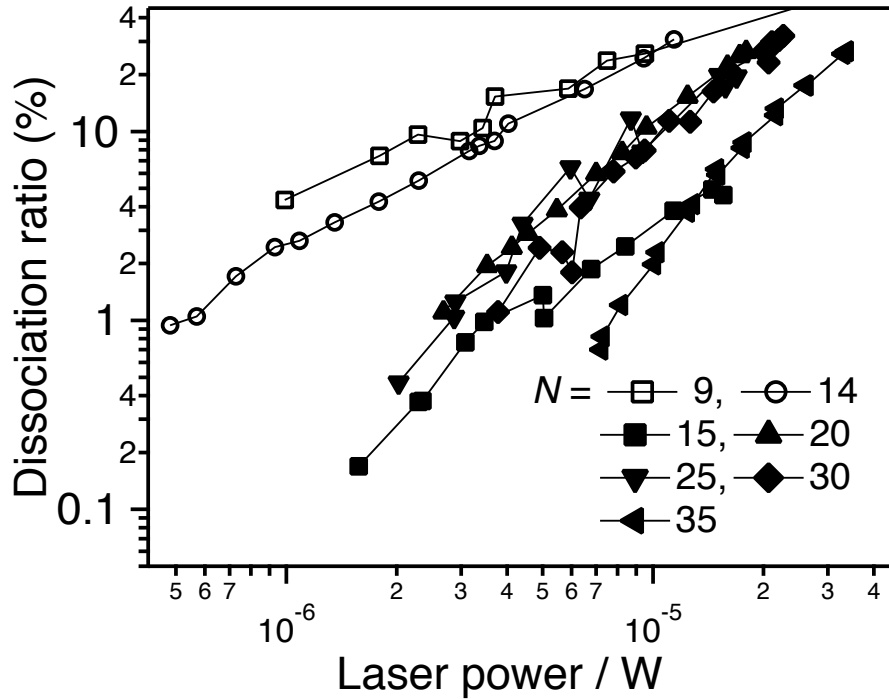
Figure 6.2: The ratio of the dissociated ions to the parent ions in the trap measured as a function of laser power in a double logarithmic plot.

6.3.2 Evaluation of photodissociation cross section

Photodissociation cross section was determined for quantitative analysis of the photoabsorption process. In the present photodissociation measurement employing an

ion trap, photodissociation cross section, σ_{PD}, is expressed as below:

$$\frac{n_{\text{dis}}}{\rho L A} = 1 - \exp\left(-\frac{\sigma_{\text{PD}} \cdot n_{\text{photon}}}{A}\right), \tag{6.1}$$

where n_{dis} is the number of dissociated ions, ρ is the number density of the parent ions, L is the interaction length, A stands for the area of the laser spot. When the amount of fragment ions is sufficiently small, Eq 6.1 can be approximated as

$$\sigma_{\text{PD}} \cong \frac{n_{\text{dis}}}{n_{\text{photon}}} \cdot \frac{1}{\rho L}. \tag{6.2}$$

In order to estimate the number density, ρ, the ion distribution in the trap was measured by scanning the laser axis over the cross section of the trap. Figure 6.3 shows photofragmentation yields of Ag_{12}^+ as a function of laser position for determination of ion distribution in the trap. The cluster ions were found to distribute in a columnar volume with a cross-sectioned diameter of $\sim$5 mm in the 11-mm diameter trap. The 1D measurement of ion distribution in the Figure 6.3 is converted to 2D data by assuming a rotational symmetry. Because the total amount of the trapped ions can be easily measured as ion currents, a column density of the ions in the laser path, ρL, was evaluated by using the 2D data of ion distribution of ions and the laser spot size A.

6.3.3 Size and temperature dependence of spectra

Photodissociation spectra of Ag_n^+ ($n = 8$–14) in the range from 3.70 to 4.35 eV are shown in Figure 6.4. Size-dependence of the spectra shows not simple energy shifts but dramatic changes in the profiles and in the peak energies. All the clusters, except for Ag_{10}^+ and Ag_{14}^+, exhibit absorption peaks in the measured energy region.
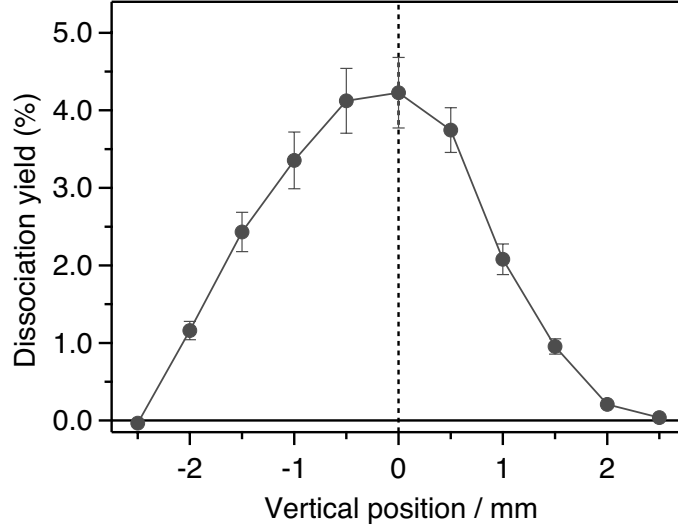
Figure 6.3: An ion distribution in the trap measured for Ag_{12}^+. The dashed line indicates the laser position when the photodissociation spectra were measured.

The observed peaks are fitted by a Gaussian function to determine peak energies and widths. Also transition intensity was quantified by an oscillator strength, which was calculated as follows [101]:

$$f = \frac{4\varepsilon_0 m_e c^2 \ln 10}{N_A e^2} \int_{\tilde{\nu}_1}^{\tilde{\nu}_2} d\tilde{\nu} \cdot \varepsilon\tilde{\nu}.$$ (6.3)

The Eq 6.3 is rewritten to a useful form of a photodissociation cross section plotted as a function of photon energy [102]:

$$f = 0.91103 \int_{\text{Peak}} dE \cdot \sigma_{\text{PD}}(E).$$ (6.4)

Here, σ_{PD} and E are in units of Å^2 and eV, respectively. The oscillator strengths thus calculated were divided by numbers of 5s-electrons in the cluster, which are listed in Table 6.1.

The peaks were broad with full widths at half maximum (FWHMs) greater than

0.1 eV. As for Ag_{10}^+ and Ag_{14}^+, the spectra were structure-less and the cross sections was smaller compared to those of the other sizes.

Table 6.1: Parameters of absorption peaks calculated for the spectra in Figure 6.4: Transition energy, FWHM of the peak, and oscillator strength (f) per 5s-electrons are listed for each peak. Values in parentheses are pro forma amount because only a part of absorption peak is measured in the measurements.

n	Transition energy / eV	FWHM / eV	f	Peak label
8	3.87	0.20	0.36	8A
9	3.78	0.12	0.044	9A
	3.92	0.12	0.10	9B
	4.09	0.11	0.089	9C
	4.21	0.072	0.12	9D
11	(3.60)	(0.20)	(0.17)	11A
	4.00	0.20	0.072	11B
	(4.30)	(0.16)	(0.16)	11C
12	3.99	0.24	0.15	12A
13	3.91	0.17	0.094	13A

The photodissociation spectra of Ag_9^+ and Ag_{12}^+ were measured also at 110 K for a temperature-dependence study and are shown in Figure 6.5. All the peaks became narrower and some of them in the Ag_9^+ spectrum were blue-shifted. However, no spectral structures were resolved. These changes are listed in Table 6.5.

6.3.4 Spectral prediction with theoretical calculations

Optical transitions of the most- and the second most- stable isomers were calculated for Ag_n^+ ($n = 8$–11) by using the TD-DFT methods. Geometrical structures of Ag_n^+ ($n = 8$–10) are shown in Figure 4.3 in Chapter 4. Calculated spectra are shown in Figure 6.6 with superimposing experimental ones.
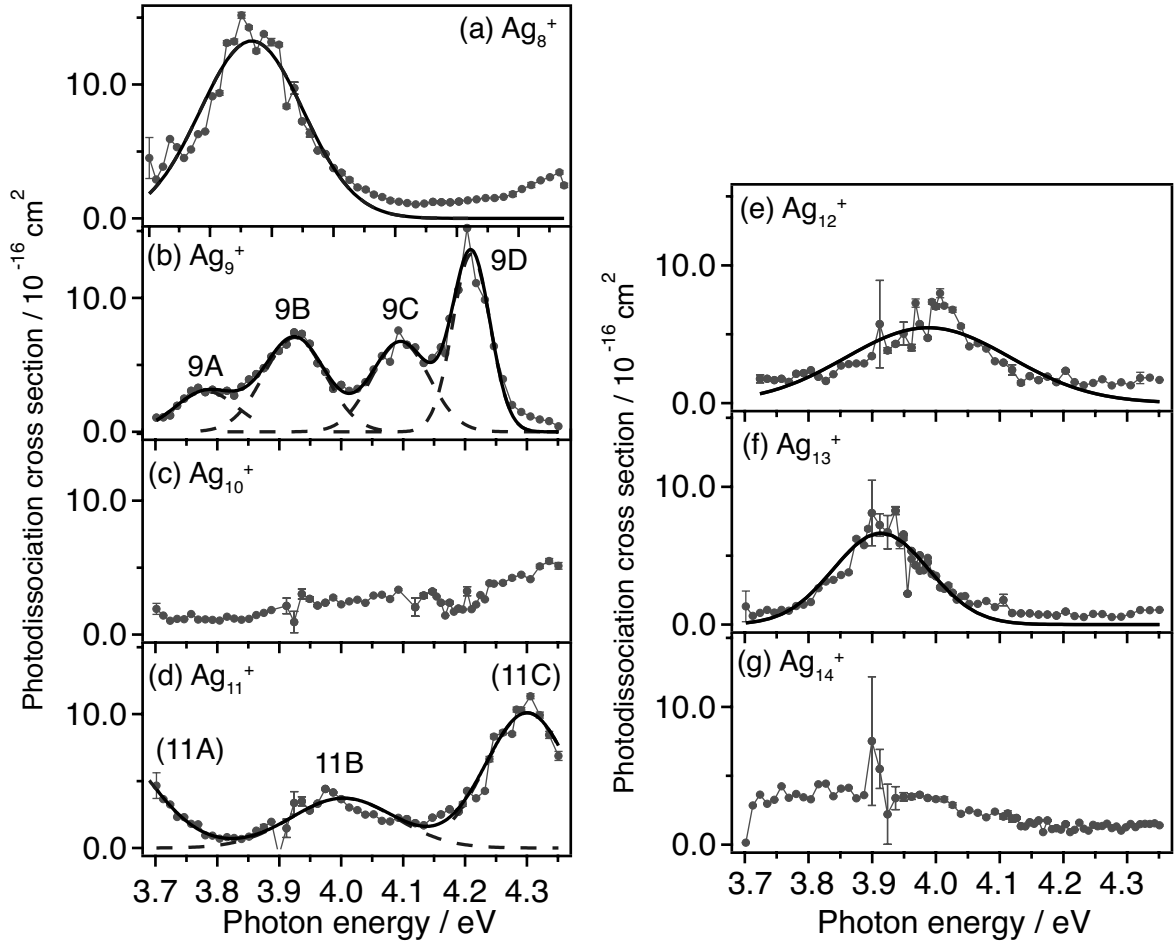
Figure 6.4: Photodissociation spectra of Ag_n^+ ($n = 8$–14) measured at 300 K.

6.4 Discussion

6.4.1 Time scale of photodissociation

Since photoabsorption is evaluated via dissociation of the parent ions in the present method, it is necessary to confirm that the photoexcited cluster ions dissociate before detection.

Here we consider pre-dissociation with an excess energy deposited by a photon, i.e., the dissociation rate estimated by the RRK theory described in Subsection 4.4.1.

66
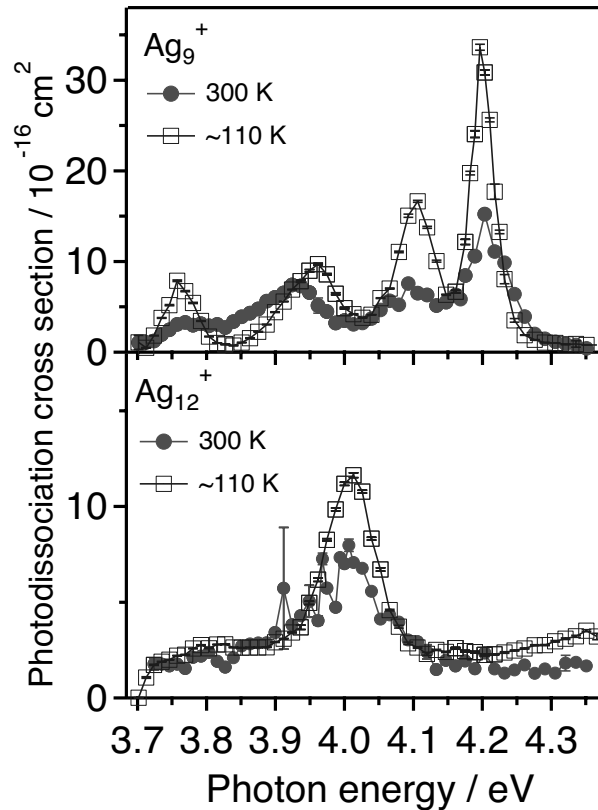
Figure 6.5: Temperature dependence of the photodissociation spectra of Ag_9^+ (top panel) and Ag_{12}^+ (bottom panel). The closed circles show data measured at 300 K. The open squares are those measured with cooling the ion trap down to 110 K.

One should note that there exist a sufficient amount of He atoms for thermalization in a few milli seconds in the trap; thermalization through collisions with the He atoms is a process competing with photodissociation.

The dissociation energies of Ag_n^+ were measured experimentally by the collision-induced-dissociation (CID) technique as reported in ref. [103]. By using these energies and RRK theory (see Subsection 4.4.1), the dissociation lifetimes after absorption of a 4.0-eV photon are estimated as in Table 6.3.

By referring to a result of molecular-dynamics simulation [35], internal temper-

Table 6.2: Energy shifts and width changes in the photodissociation spectra of Ag_9^+ and Ag_{12}^+ in 110 K with respect to those at 300 K. Negative values of ΔFWHM mean sharpening of the peaks by cooling; all the peaks became narrower at 110 K.

n	Peak label	Energy shift / meV	ΔFWHM (%)
9	9A	-19	-52
	9B	+29	-8.0
	9C	+0.8	-32
	9D	-9.6	-40
12	12A	+20	-9

Table 6.3: Dissociation energy of Ag atom from Ag_n^+ and estimated lifetime after absorbing 4.0-eV photon.

Size n	Dissociation energy [103]	Lifetime / μs
8	2.19	0.00190
9	2.95	13.8
10	1.58	0.000351
11	2.14	0.129
12	1.87	0.0353
13	2.41	47.7
14	2.00	1.40
15	2.51	36.16

ature of a cluster, T_{cluster}, after x collisions can be estimated as

$$T_{\text{cluster}}(x) = (T_{\text{cluster}}(0) - T_{\text{He}}) \cdot \left(1 - \frac{K}{3nk_{\text{B}}}\right)^x + T_{\text{He}}, \qquad (6.5)$$

where T_{He} is the temperature of the buffer gas, K is the energy exchange constant (assumed to be 2.8 μeV $\cdot$ K^{-1}). On the basis of Eq 6.5, the decay rates of the excess energies (the cooling rates) of Ag_{10}^+ and Ag_{13}^+, which have the shortest and the longest lifetime, respectively, are calculated as in Figure 6.7. Since the thermalization rates are in the milli-second scale, thermalization indeed competes with

the dissociation and causes underestimation of the photodissociation cross section through de-excitation of the cluster ions via collision with a He gas in the trap.

Since the spectra were measured as photodissociation spectra, one might overestimate the photodissociation cross sections due to the presence of two-photon dissociation processes. According to the results shown in Figure 6.2, photofragment yields of Ag_n^+ ($n = 9$, 14) increase linearly with the laser fluence. Therefore, the photodissociation spectra shown in Figure 6.4 can therefore be attributed to one-photon processes. However, photofragment yields of the larger cluster (Ag_n^+, $n > 14$) increased quadratically, i.e., photodissociation of Ag_n^+ ($n > 14$) occurred via two-photon processes. This can be interpreted as photoabsorption of the excited clusters, which was generated by the first photon, because of their longer lifetimes.

6.4.2   Assignment of optical transitions

$\mathbf{Ag_8^+}$. The broadest peak was observed among the size ($n = 8$–14), even though Ag_8^+ is the smallest size investigated. Many electronic transitions were predicted in the theoretical results in the range of 3.6–4.2 eV as shown in Figure 6.6 (a). The broad feature of peak 8A is thus attributed to unresolved several electronic transitions located closely.

$\mathbf{Ag_9^+}$. Four peaks in Figure 6.4 (b) are completely different from previously reported photodissociation spectra of free Ag_9^+ [11, 12], which show a very broad absorption band (FWHM = 0.62 eV) at 4.02 eV. They measured the spectra by photodepletion of Ag_9^+ ion beam, and estimated internal energy of Ag_9^+ to be in 1000–2000 K as prepared by pulsed-arc discharge at a very high temperature. On the other hand, the spectrum in Figure 6.4 are measured under the thermalized condition at 300 K. Therefore, the difference is ascribed to thermal broadening of the spectrum at high temperatures.

As shown in Figure 6.5, the peaks became narrower and blue-shifted when the ion trap was cooled down to 110 K. Since no peaks disappeared at 110 K, all the peaks originate from transitions to different electronic excited states rather than vibrational structures.

Vibrational populations were simulated for the lowest vibration frequency of Ag_9^+ (structure 9-I), which was calculated to be 45 cm^{-1}, as shown in Figure 6.8. Almost 50% of the ions are populated in the vibrational ground state at 110 K, while 20% of ions at 300 K. Therefore, the narrowing of the peaks can be explained by a population shift to lower vibration levels. In other words, the peaks at 300 K are due to hot-band contributions. The difference between the spectrum at the room temperature and that measured at 110 K is a typical feature of molecular-like absorption.

TD-DFT calculations reproduce well the features of the experimental spectrum of Ag_9^+ as shown in Figure 6.6 (b). For instance, the experimental peak 9A at 3.78 eV is explained by the result of TD-DFT for the most stable isomer (9-I), which shows the transitions at 3.76, 3.83, and 3.78 eV by B3LYP, LC-ωPBE, and CAM-B3LYP, respectively. In a similar way, the peak 9B can be assigned the transition of the second most stable isomer (9-II), which is located at 3.93 (B3LYP), 3.90 (LC-ωPBE), and 4.01 (CAM-B3LYP) eV. Therefore, it is speculated that both the isomers, 9-I and 9-II, coexist in the trap. Since there are several predicted transitions around 4.2 eV in each calculation level, the peak 9D, which is more intense than the others, may be composed of more than one electronic transitions.

Ag_{10}^+. The structureless spectrum of Ag_{10}^+ in Figure 6.4 (c) suggests that photoabsorption of Ag_{10}^+ is not measurable by action spectroscopy via photodissociation, i.e., the cluster ions may not dissociate after photoabsorption. Since the photodissociation cross section increases with the photon energy, it looks as if the cluster ions

would not dissociate until they acquire a sufficient excess energy. However, as shown by the result of theoretical calculations in Figure 6.6 (c), no optical transitions were predicted in the region of 3.7–4.1 eV for the most stable isomer of Ag_{10}^+ by any of the three calculation levels. In addition, there are several transitions in the range of 4.1–4.3 eV. It is therefore presumed that the photodissociation signal increasing with the photon energy is due to the tail of the broadened transitions present at around 4.2 eV.

Ag_{11}^+. The photodissociation spectrum shows (Figure 6.4 (d)) three very broad bands with FWHMs similar to that of Ag_8^+. However, the TD-DFT calculations (Figure 6.6 (d)) predicted many electronic transitions in the measurement range. The increase in the number of excited states can be considered as a result of increase in the number of atoms and degrees of freedom, which results in a high density of states. Therefore, it cannot be ruled out the possibility that these bands consist of more than two electronic transitions.

Ag_{14}^+. The photodissociation cross section decreases with the photon energy in the Ag_{14}^+ spectrum shown in Figure 6.4 (g). It can be ruled out a situation that dissociation did not occur because of lack of an excess energy. In addition, since the photofragment yield increased linearly with the photon flux as described in Subsection 6.4.1, it was confirmed that one-photon energy is sufficient for photodissociation of Ag_{14}^+.

Surface plasmon resonant absorption of silver nano particles has been reported as listed in Table 6.4. The widths (FWHM) of surface plasmon absorption are broader than 0.2 eV, while the observed peaks of Ag_9^+ are narrower than 0.15 eV. Therefore, the obtained absorption peaks of Ag_9^+ can be attributed to the molecular-like excitation. Although the widths of Ag_n^+ ($n = 8$, 10–14) are around 0.2 eV, these peaks cannot be ascribed to plasmon-like excitation because the peaks may consist

Table 6.4: Optical absorption properties of silver nano particles.

Excitation energy / eV	FWHM / eV	Oscillator strength per atom	Particle diameter
3.3 [85]	0.2	0.2	20 nm
2.9 [104]	0.28	0.3	400 nm
4.0 [105]	0.5		3.65 nm

of several electronic transitions between molecular orbitals. The oscillator strengths per 5s-electron of the clusters are less than 0.1 except for 8A and 12A, which again may be composed of clump of transitions, while that of reported plasmon absorption is greater than 0.2. Therefore, by inferring from lower oscillator strengths of the clusters, these are concluded to be molecular-like absorption, i.e., the intensities of absorption are too weak compared to the plasmon resonance.

6.5 Summary

Photoabsorption of Ag_n^+ ($n = 8$–35) in the range of 3.70–4.35 eV was investigated by means of photodissociation spectroscopy. As for Ag_n^+ ($n = 8$–14), photodissociation occurred by the one photon process, and size-dependent spectra were obtained. By referring to the spectral peak widths and the oscillator strengths per 5s-electron, these absorption peaks were characterized as molecular-like absorption, i.e., absorption was resulted from the electronic transition between the two states. On the other hand, photodissociation of Ag_n^+ ($n \geqq 15$) by UV photons was found to be dominated by multiple photon processes, because the fragmentation yield increased quadratically with the number of photon.
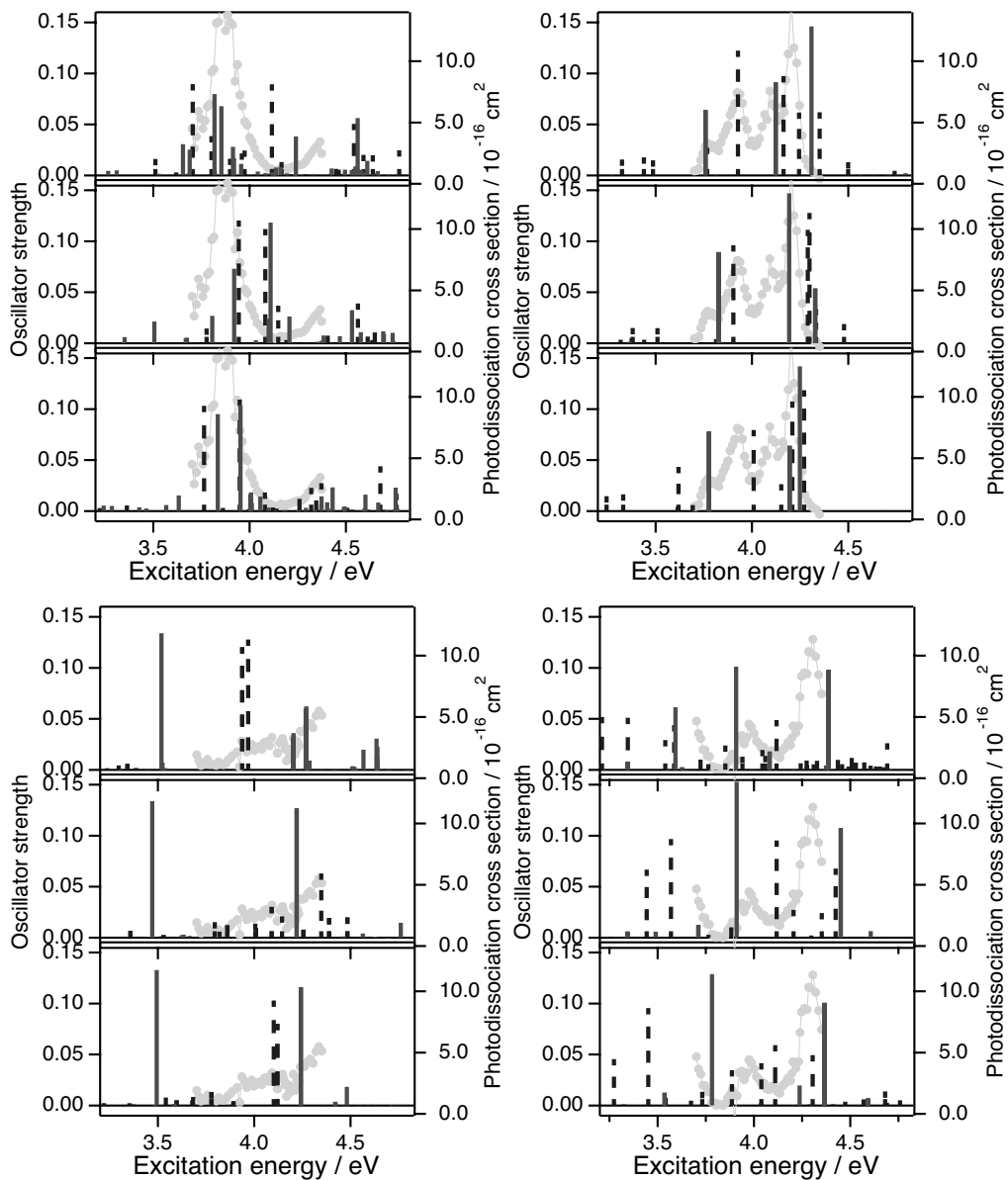
Figure 6.6: Optical transitions calculated by TD-DFT for (a) Ag_8^+, (b) Ag_9^+, (c) Ag_{10}^+, and (d) Ag_{11}^+. (Top panel) B3LYP / modified LANL2DZ, (Middle panel) LC-ωPBE / Def2-TZVPP, (Bottom panel) CAM-B3LYP / Def2-TZVPP. Solid lines are transitions of the most stable isomer, and dashed lines are that of the second most stable isomer. Experimental results are superimposed.

73
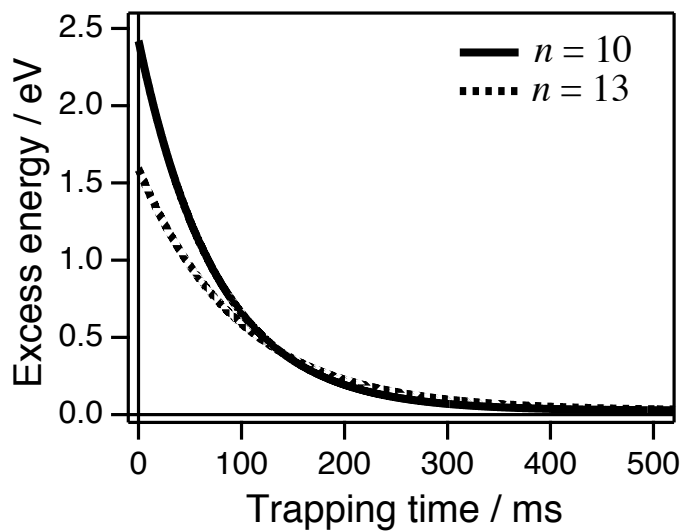
Figure 6.7: Thermalization rates of Ag_{10}^+ and Ag_{13}^+ calculated by Eq 6.5. The pressure of the buffer He gas is assumed to be 0.1 Pa.
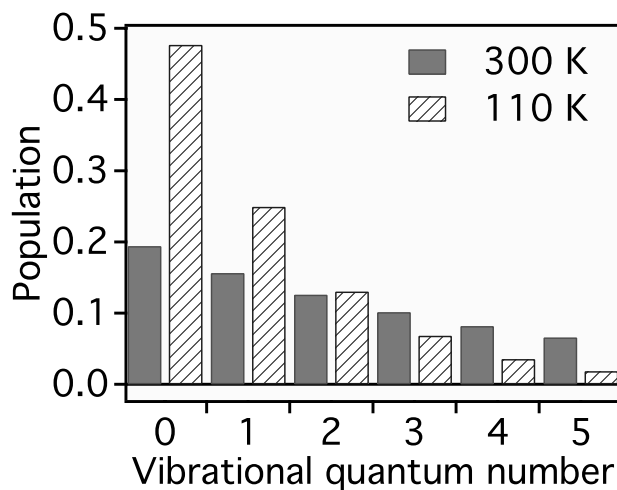
Figure 6.8: Vibrational populations of Ag_9^+ (9-I). Solid bars represent populations at 300 K, while striped bars are those of 110 K.

Chapter 7

Concluding remarks

The reaction kinetics and the optical absorption of the transition metal clusters were investigated by employing an ion trap, which provided controlled experimental conditions for kinetics and spectroscopic measurements of cluster ions. As for reaction measurement, the method enabled us to control the number of collisions with reactant molecules, by adjusting either the concentration of the reactant gas or the storage time of the cluster ions. The reaction kinetics are deduced by the control of the storage time in the trap. The advantages of the method in spectroscopic measurement are capabilities of evaluating the number density of the target cluster ion for laser irradiation as well as temperature control of the ions via thermalization with the buffer He gas. Photoabsorption cross sections can thus be determined accurately.

The reaction rate constants of each pathway, including reaction intermediates, were determined even for branched pathways as described in Chapter 3. The oxidation of both Cr_2^+ and Cr_3^+ were found to result in generation of Cr^+ and CrO^+ with a branching ratio of $[Cr^+] : [CrO^+] \approx 3 : 1$, although the production mechanism of CrO^+ was different. Cr_2^+ produced CrO^+ directly, whereas Cr_3^+ produced $\sim 80\%$ of CrO^+ via intermediates, Cr_2^+ and Cr_2O^+. The reaction cross section of the most minor intermediate in the reaction of Cr_3^+, whose branching ratio was only 1.3%, was

able to be determined successfully due to the high sensitivity of the present technique. Moreover, the fact that the cross sections of the reactant $Cr_2{}^+$ and Cr_2O^+ were nearly equal to those of the intermediates in the reaction of Cr_3^+ demonstrates that the reaction-intermediate ions are well thermalized with the buffer He gas.

The sequential adsorption of dinitrogens on Ag_n^+ ($n = 1$–10) was investigated in Chapter 4 by taking an advantage of the ion-trap experiment. The adsorption of N_2 was observed only when the clusters were cooled down through the collisions with a buffer He gas at 120 K; no adsorption was observed at room temperature. Geometrical structures of bare Ag_n^+ and their N_2 adducts were deduced from the numbers of N_2 molecules adsorbed on Ag_n^+ at 105 K, and are supported further structures obtained by DFT calculations. The adsorption site of Ag_n^+ was determined as well, which provides information about reaction mechanisms with other molecules such as CO because molecular adsorption is the primary step of ion–molecule reactions.

Chapter 5 presented reaction kinetics of Au_2^+ with CO and O_2. In order to elucidate an ability of foreign molecules to control the reactivity of Au_2^+, reactions of Au_2X^+ (X = H_2O, MeOH, and CO) were investigated as well. Preadsorption of a molecule either H_2O or MeOH on Au_2^+ leads to enhancement (by a factor of 210 or 730) of CO adsorption due to an increased rate of Au–Au bond cleavage as well as to release of the the pre-adsorbed molecule to liberate an excess internal energy upon reaction; the former can be attributed to the weakened Au–Au bond caused by adsorption of the pre-adsorbed molecule. Preadsorption of a H_2O or CO molecule on Au_2^+ initiated adsorption of up to two molecules of O_2. This enhancement and initiation of the reactions by H_2O (or CO) were caused by partial electron transfer from the O atom in the coadsorbed H_2O (or from the C atom in CO) to Au_2^+. These results demonstrated the possibility of controlling reactivity of clusters by attachment of foreign molecules.

Optical absorption spectroscopy of Ag_n^+ ($n = 8$–14) in the range of 3.70–4.35 eV was performed for investigation of optical properties and photodissociation processes. Photodissociation of Ag_n^+ ($n = 8$–14) was found to be a one-photon process, where an action spectrum of photodissociation was able to be interpreted as a photoabsorption spectrum. These spectra exhibited a clear dependence on the cluster size. By judging from the spectral peak width and the oscillator strength per 5s-electron, these photoexcitation processes were characterized as a single-electron transition between two electronic states, which is in striking contrast to a plasmonic transition involving collective excitation of many electrons observed commonly in larger silver nano particles.

In this thesis, the reaction and the optical absorption of clusters were presented under the conditions with the existence of the buffer He gas. This technique allows us to investigate chemical and physical properties of clusters under the bridging condition between a gas phase and a liquid phase, i.e., the cluster can interact with He during the reaction of photoabsorption, and is no longer isolated. Investigation of reactive sites in clusters, which is demonstrated in Chapter 4, would contribute to material design with making use of clusters. Even though all the measurements were performed in the course of energy exchange with the buffer He gas, considering a practical use of properties of clusters, a systematic study of interaction with surroundings, such as a supporting substrate and protecting groups, will be useful. The coadsorption effect of only one molecule were demonstrated in Chapter 5, which should be extended to multi-molecular systems in order to bridge between the gas phase and the liquid phase. The first step of this idea would be investigation of properties of clusters, which is embedded in a liquid droplet measured in the gas phase. The author believes that the study demonstrated in the thesis provides knowledge not only for molecular science but also for material science.

References

[1] W. A. de Heer, *Rev. Mod. Phys.* **65**, 611 (1993).

[2] R. Kubo, *Phys. Lett.* **1**, 49 (1962).

[3] P. B. Armentrout, *Int. J. Mass Spectrom.* **200**, 219 (2000).

[4] T. M. Bernhardt, *Int. J. Mass Spectrom.* **243**, 1 (2005).

[5] L. D. Socaciu, J. Hagen, T. M. Bernhardt, L. Wöste, U. Heiz, H. Häkkinen, U. Landman, *J. Am. Chem. Soc.* **125**, 10437 (2003).

[6] T. M. Bernhardt, L. D. Socaciu-Siebert, J. Hagen, L. Wöste, *Appl. Catal., A* **291**, 170 (2005).

[7] S. M. Lang, T. Bernhardt, R. Barnett, U. Landman, *Angew. Chem., Int. Ed.* **49**, 980 (2010).

[8] S. M. Lang, T. Bernhardt, R. Barnett, U. Landman, *J. Chem. Phys. C* **115**, 6788 (2011).

[9] M. Harb, F. Rabilloud, D. Simon, A. Rydlo, S. Lecoultre, F. Conus, V. Rodrigues, C. Félix, *J. Chem. Phys.* **129**, 194108 (2008).

[10] S. Lecoultre, A. Rydlo, C. Félix, J. Buttet, S. Gilb, W. Harbich, *J. Chem. Phys.* **134**, 074302 (2011).

[11] J. Tiggesbäumker, L. Köller, H. Lutz, K. Meiwes-Broer, *Chem. Phys. Lett.* **190**, 42 (1992).

[12] J. Tiggesbäumker, L. Köller, K. Meiwes-Broer, A. Liebsch, *Phys. Rev. A* **48**, R1749 (1993).

[13] S. Haupt, J. Kaller, D. Schooss, D. Cameron, M. M. Kappes, *Z. Phys. D.* **40**, 331 (1997).

[14] A. N. Gloess, H. Schneider, J. Weber, M. M. Kappes, *J. Chem. Phys.* **128**, 114312 (2008).

[15] D. Schooss, S. Gilb, J. Kaller, M. M. Kappes, F. Furche, A. Köhn, K. May, R. Ahlrichs, *J. Chem. Phys.* **113** (2000).

[16] A. Shayeghi, R. L. Johnston, R. Schäfer, *Phys. Chem. Chem. Phys.* **15**, 19715 (2013).

[17] A. Shayeghi, C. J. Heard, R. L. Johnston, R. Schäfer, *J. Chem. Phys.* **140**, 054312 (2014).

[18] T. Majima, G. Santambrogio, C. Bartels, A. Terasaki, T. Kondow, J. Meinen, T. Leisner, *Phys. Rev. A* **85**, 053414 (2012).

[19] R. M. Jones, D. Gerlich, S. L. Anderson, *Rev. Sci. Instrum* **68**, 3357 (1997).

[20] M. J. Frisch, *et al.*, Gaussian09 Revision C.01. Gaussian Inc. Wallingford CT 2009.

[21] M. A. Korotin, V. I. Anisimov, D. I. Khomskii, G. A. Sawatzky, *Phys. Rev. Lett.* **80**, 4305 (1998).

[22] S. Casey, D. Leopold, *J. Phys. Chem.* **97**, 816 (1993).

[23] K. Tono, A. Terasaki, T. Ohta, T. Kondow, *J. Chem. Phys.* **119**, 11221 (2003).

[24] K. Tono, A. Terasaki, T. Ohta, T. Kondow, *Phys. Rev. Lett.* **90**, 133402 (2003).

[25] B. Reddy, S. Khanna, *Phys. Rev. Lett.* **83**, 3170 (1999).

[26] B. Reddy, S. Khanna, C. Ashman, *Phys. Rev. B* **61**, 5797 (2000).

[27] X. Wang, S. Neukermans, F. Vanhoutte, E. Janssens, G. Verschoren, R. Silverans, P. Lievens, *Appl. Phys. B* **73**, 417 (2001).

[28] J. Griffin, P. Armentrout, *J. Chem. Phys.* **108**, 8062 (1998).

[29] L. Socaciu, J. Hagen, U. Heiz, T. Bernhardt, T. Leisner, L. Wöste, *Chem. Phys. Lett.* **2001**, 282 (340).

[30] T. Ito, K. Egashira, K. Tsukiyama, A. Terasaki, *Chem. Phys. Lett.* **538**, 19 (2012).

[31] G. Gioumousis, D. P. Stevenson, *J. Chem. Phys.* **29**, 294 (1958).

[32] A. Fiedler, I. Kretzschmar, D. Schr?der, H. Schwarz, *J. Am. Chem. Soc.* **118**, 9941 (1996).

[33] E. Fisher, J. Elkind, D. Clemmer, R. Georgiadis, S. Loh, N. Aristov, L. Sunderlin, P. Armentrout, *J. Chem. Phys.* **93**, 2676 (1990).

[34] F. Aubriet, B. Maunit, B. Courrier, J. Muller, *Rapid Commun. Mass Spectrom.* **11**, 1596 (1997).

[35] J. Westergren, H. Grönbeck, S.-G. Kim, D. Tománek, *J. Chem. Phys.* **107**, 3071 (1997).

[36] D. Bergeron, A. Castleman, Jr., N. Jones, S. Khanna, *Nano Lett.* **4**, 261 (2004).

[37] C.-X. Su, D. Hales, P. Armentrout, *Chem. Phys. Lett.* **201**, 199 (1993).

[38] K. Molek, Z. Reed, A. Ricks, M. Duncan, *J. Phys. Chem. A* **111**, 8080 (2007).

[39] R. Levine, *Molecular Reaction Dynamics* (Cambridge University Press, 2005).

[40] M. Haruta, T. Kobayashi, H. Sano, N. Yamada, *Chemistry Letters* **16**, 405 (1987).

[41] P. J. Roach, W. H. Woodward, A. W. Castleman, A. C. Reber, S. N. Khanna, *Science* **323**, 492 (2009).

[42] W. H. Woodward, A. C. Reber, J. C. Smith, S. N. Khanna, A. W. Castleman, *J. Phys.Chem. C* **117**, 7445 (2013).

[43] V. Bonačić-Koutecký, L. Češpiva, P. Fantucci, J. Koutecký, *J. Chem. Phys.* **98**, 7981 (1993).

[44] M. J. Manard, P. R. Kemper, M. T. Bowers, *J. Am. Chem. Soc.* **127**, 9994 (2005).

[45] Y. N. Wu, M. Schmidt, J. Leygnier, H. P. Cheng, A. Masson, C. Bréchignac, *J. Chem. Phys.* **136**, 024314 (2012).

[46] M. Schmidt, A. Masson, C. Bréchignac, *J. Chem. Phys.* **122**, 134712 (2005).

[47] M. Schmidt, P. Cahuzac, C. Bréchignac, H. Cheng, *J. Chem. Phys.* **118**, 10956 (2003).

[48] M. Schmidt, A. Masson, C. Bréchignac, *Phys. Rev. Lett.* **91**, 243401 (2003).

[49] X. Wu, L. Senapati, S. K. Nayak, A. Selloni, M. Hajaligol, *J. Chem. Phys.* **117** (2002).

[50] A. Terasaki, T. Majima, C. Kasai, T. Kondow, *The European Physical Journal D* **52** (2009).

[51] A. D. Becke, *J. Chem. Phys.* **98**, 5648 (1993).

[52] C. Lee, W. Yang, R. G. Parr, *Phys. Rev. B* **37**, 785 (1988).

[53] M. Couty, M. B. Hall, *J. Comp. Chem.* **17**, 1359 (1996).

[54] E. Schumacher, *DETMECH - Chemical Reaction Kinetics Software* (2009).

[55] J. Silva, C. Stampfl, M. Scheffler, *Phys. Rev. Lett.* **90**, 066104 (2003).

[56] M. Haruta, N. Yamada, T. Kobayashi, S. Iijima, *J. Catal.* **115**, 301 (1989).

[57] A. Corma, H. Garcia, *Chem. Soc. Rev.* **37**, 2096 (2008).

[58] M. Stratakis, H. Garcia, *Chem. Rev.* **112**, 4469 (2012).

[59] J. Guzman, B. C. Gates, *J. Am. Chem. Soc.* **126**, 2672 (2004).

[60] A. A. Herzing, C. J. Kiely, A. F. Carley, L. P., H. G. J., *Science* **321**, 1331 (2008).

[61] S. D. Lin, M. Bollinger, V. M. A., *Catal. Lett.* **17**, 245 (1993).

[62] S. Arrii, F. Morfin, A. J. Renouprez, J. L. Rousset, *J. Am. Chem. Soc.* **126**, 1199 (2004).

[63] G. N. Vayssilov, B. C. Gates, N. Rösch, *Angew. Chem. Int. Ed.* **42**, 1391 (2003).

[64] A. Sanchez, S. Abbet, U. Heiz, W.-D. Schneider, H. Häkkinen, R. N. Barnett, U. Landman, *J. Phys. Chem. A* **103**, 9573 (1999).

[65] W. Ruettinger, O. Ilinich, R. J. Farrauto, *J. Power Sources* **118**, 61 (2003).

[66] S. M. Lang, T. M. Bernhardt, *Faraday Discuss.* **152**, 337 (2011).

[67] Y. Wang, D. Zhang, R. Zhu, C. Zhang, C. Liu, *J. Phys. Chem. C* **113**, 6215 (2009).

[68] D. M. Popolan, M. Nössler, R. Mitrić, T. M. Bernhardt, V. Bonačić-Koutecký, *J. Phys. Chem. A* **115**, 951 (2011).

[69] M. Daté, M. Haruta, *J. Catal.* **201**, 221 (2001).

[70] M. Daté, M. Okumura, S. Tsubota, M. Haruta, *Angew. Chem. Int. Ed.* **43**, 2129 (2004).

[71] W. T. Wallace, R. B. Wrywas, A. J. Leavitt, R. L. Wheten, *Phys. Chem. Chem. Phys.* **7**, 930 (2005).

[72] W. T. Wallace, R. B. Wrywas, R. L. Wheten, R. Mitriý, V. Bonačić-Koutecký, *J. Am. Chem. Soc.* **125**, 8408 (2003).

[73] W. T. Wallace, R. L. Whetten, *J. Am. Chem. Soc.* **124**, 7499 (2002).

[74] S. M. Lang, T. M. Bernhardt, R. N. Barnett, B. Yoon, U. Landman, *J. Am. Chem. Soc.* **131**, 8939 (2009).

[75] M. Neumaier, F. Weigend, O. Hampe, M. M. Kappes, *J. Chem. Phys.* **122**, 1 (2005).

[76] D. M. Cox, R. Brickman, K. Creegan, A. Kaldor, *Z. Phys. D* **19**, 353 (1991).

[77] T. Su, M. T. Bowers, *J. Chem. Phys.* **58**, 3027 (1973).

[78] T. Su, M. T. Bowers, *Int. J. Mass Spectrom. Ion Processes* **12**, 347 (1973).

[79] S. Becker, G. Dietrich, H.-U. Hasse, N. Klisch, H.-J. Kluge, D. Kreisle, S. Krückeberg, M. Lindinger, K. Lützenkirchen, L. Schweikhard, H. Weidele, J. Ziegler, *Z. Phys. D.* **30**, 341 (1994).

[80] H. Häkkinen, U. Landman, *J. Am. Chem. Soc.* **123**, 9704 (2001).

[81] A. P. Woodham, G. Meijer, A. Fielicke, *J. Am. Chem. Soc.* **135**, 1727 (2013).

[82] G. Papavassiliou, *Progress in Solid State Chemistry* **12**, 185 (1979).

[83] C. F. A. Negre, C. G. Sáchez, *J. Chem. Phys.* **129**, 034710 (2008).

[84] P. Mulvaney, *Langmuir* **12**, 788 (1996).

[85] S. Link, Z. L. Wang, M. A. El-Sayed, *J. Phys. Chem. B* **103**, 3529 (1999).

[86] E. Ringe, J. M. McMahon, K. Sohn, C. M. Cobley, Y. Xia, J. Huang, G. C. Schatz, L. D. Marks, R. P. Van Duyne, *J. Phys. Chem. C* **114**, 12511 (2010).

[87] E. Ringe, J. Zhang, M. R. Langille, K. Sohn, C. M. Cobley, L. Au, Y. Xia, C. A. Mirkin, J. Huang, L. D. Marks, R. P. Van Duyne, *Mater. Res. Soc. Symp. Proc.* **1208**, O10 (2010).

[88] E. Ringe, M. R. Langille, K. Sohn, J. Zhang, J. Huang, C. A. Mirkin, R. P. Van Duyne, L. D. Marks, *J. Phys. Chem. Lett.* **3**, 1479 (2012).

[89] E. Ringe, B. Sharma, A.-I. Henry, L. D. Marks, R. P. Van Duyne, *Phys. Chem. Chem. Phys.* **15**, 4110 (2013).

[90] K. L. Kelly, E. Coronado, L. L. Zhao, G. C. Schatz, *J. Phys. Chem. B* **107**, 668 (2003).

[91] C. M. Aikens, S. Li, G. C. Schatz, *J. Phys. Chem. C* **112**, 11272 (2008).

[92] J. Idrobo, W. Walkosz, S. Yip, S. Öğüt, J. Wang, J. Jellinek, *Phys. Rev. B* **76**, 205422 (2007).

[93] S. Fedrigo, W. Harbich, J. Buttet, *Phys. Rev. B* **47**, 10706 (1993).

[94] R. Antoine, T. Tabarin, M. Broyer, P. Dugourd, R. Mitrić, V. Bonačić-Koutecký, *Chem. Phys. Chem.* **7**, 524 (2006).

[95] R. Mitrić, J. Petersen, A. Kulesza, V. Bonačić-Koutecký, T. Tabarin, I. Compagnon, R. Antoine, M. Broyer, P. Dugourd, *J. Chem. Phys.* **127**, 134301 (2007).

[96] T. Tabarin, A. Kulesza, R. Antoine, R. Mitrić, M. Broyer, P. Dugourd, V. Bonačić-Koutecký, *Phys. Rev. Lett.* **101**, 213001 (2008).

[97] L. Gell, A. Kulesza, J. Petersen, M. I. S. Röhr, R. Mitrić, V. Bonačić-Koutecký, *J. Phys. Chem. C* **117**, 14824 (2013).

[98] J. C. Idrobo, S. Öğüt, K. Nemeth, J. Jellinek, R. Ferrando, *Phys. Rev. B* **75**, 233411 (2007).

[99] J. C. Idrobo, S. Öğüt, J. Jellinek, *Phys. Rev. B* **72**, 085445 (2005).

[100] U. Hild, G. Dietrich, S. Krückeberg, M. Lindinger, K. Lüzenkirchen, L. Schweikhard, C. Walther, J. Ziegler, *Phys. Rev. A* **57**, 2786 (1998).

[101] J. M. Hollas, *Modern Spectroscopy Fourth Edition* (John Wiley & Sons, Ltd, 2003).

[102] J. Friedrich, S. Gilb, O. T. Ehrler, A. Behrendt, M. M. Kappes, *J. Chem. Phys.* **117**, 2635 (2002).

[103] S. Krückeberg, G. Dietrich, L. Schweikhard, C. Walther, J. Ziegler, *J. Chem. Phys.* **110**, 7216 (1999).

[104] T. R. Jensen, M. D. Malinsky, C. L. Haynes, R. P. Van Duyne, *J. Phys. Chem. B* **104**, 10549 (2000).

[105] W.-J. Yoon, K.-Y. Jung, J. Liu, T. Duraisamy, R. Revur, F. L. Teixeira, S. Sengupta, P. R. Berger, *Sol. Energy Mater. Sol. Cells* **94**, 128 (2010).

List of Publications

[1] **T. Ito**, K. Egashira, K. Tsukiyama, and A. Terasaki
Oxidation processes of chromium dimer and trimer cations in an ion trap
Chem. Phys. Lett. **538**, 19 (2012).

[2] **T. Ito**, G. N. Patwari, M. Arakawa, and A. Terasaki
Water-Induced Adsorption of Carbon Monoxide and Oxygen on the Gold Dimer Cation
J. Phys. Chem. A **118**, 8293 (2014).

[3] **T. Ito**, Y. Taniguchi, M. Arakawa, and A. Terasaki
Adsorption kinetics of nitrogen molecules on size-selected silver cluster cations
Manuscript under Preparation

[4] **T. Ito**, K. Tobita, M. Arakawa, and A. Terasaki
Photodissociation spectroscopy of size-selected silver cluster cations in a temperature-controlled ion trap
Manuscript under Preparation

[5] G. N. Patwari, **T. Ito**, K. Egashira, and A. Terasaki
Probing Structures of Small Gold Cluster Cations with Dinitrogen
Chem. Asian J. **6**, 1834 (2011). **(Not part of the Thesis)**

[6] M. Arakawa, K. Kohara, **T. Ito**, and A. Terasaki
Size-dependent reactivity of aluminum cluster cations toward water molecules
Eur. Phys. J. D **67**, 80-1–6 (2013). **(Not part of the Thesis)**